Dalton Transactions

An international journal of inorganic chemistry

This article can be cited before page numbers have been issued, to do this please use: X. Ouyang, M. Yao and T. Yang, *Dalton Trans.*, 2025, DOI: 10.1039/D5DT01206F.

Volume 46
Number 10
14 March 2017
Pages 3073-3412

Dalton Transactions

An international journal of inorganic chemistry

rsc.li/dalton

ISSN 0306-0012

ROYAL SOCIETY OF CHEMISTRY

COMMUNICATION
Douglas W. Stephen *et al.*
N-Heterocyclic carbene stabilized parent sulfenyl, selenenyl, and tellurenyl cations (XH+; X = S, Se, Te)

DOI: 10.1039/D5DT01206F

Comparative Investigation and Mechanistic Analysis of Textured PMN-30PT Ceramics Using $BaTiO_3$ and $PbTiO_3$ templates

Xi Ouyang[a,b], Manwen Yao[a,*], Tongqing Yang[a]

[a] Functional Materials Research Laboratory, School of Materials Science & Engineering, Tongji University, No. 4800, Cao'an Road, Shanghai 201804, China

[b] School of Architecture and Engineering, Jinggangshan University, Ji'an 343009, China

[*]Corresponding author. Tel numbers: +86 15026662692 CHN

E-mail address: yaomw@tongji.edu.cn (Manwen Yao).

Abstract: Homogeneous $PbTiO_3$ (PT) templates are considered an ideal choice for textured lead-based piezoceramics. In order to further investigate the texture mechanism and topological microcrystal conversion of PT templates, a comparative investigation and mechanistic analysis were conducted on $Pb(Mg_{1/3}Nb_{2/3})O_3$-30$PbTiO_3$ (PMN-30PT) textured ceramics prepared using the template grain growth (TGG) technique, with <001> oriented $BaTiO_3$ (BT) and $PbTiO_3$ (PT) as templates. The results show that the use of BT templates resulted in a textured ceramic with a Logtering factor of 91%, a piezoelectric coefficient of 824 pC/N, and parallel striped domains, compared to 11%, 534 pC/N, and fingerprint-like domains with PT templates. However, the PT templates have poor morphology and structural instability. This is due to the chaotic substitution of Bi^{3+} with Pb^{2+} and interlayer detachment at the 4a position during the topochemical conversion process, which results in the formation of PT nanosheets. At the same time the residues of Bi^{3+} lead to the formation of a more complex Aurivillius structure and allow PT templates to be embedded in this structure. Additionally, the lower formation energy, the increased lattice parameter difference, and the lower melting point of PT templates make them more susceptible diffusion into the matrix grain. Based on this comprehensive analysis, it can be concluded that achieving textured piezoceramics with PT templates is a challenging task.

Keywords: PMN-PT; Template Grain Growth; $PbTiO_3$ Template; Texture ceramics; Topochemical microcrystal conversion

1. Introduction

Template Grain Growth (TGG) is a technique utilized to produce textured ceramics with plate-like templates[1–4]. These textured ceramics are highly desirable due to their excellent piezoelectric properties. The selection of the template material is crucial in the fabrication of textured ceramics[5]. Currently, $BaTiO_3$ (BT)[6–8] and $SrTiO_3$ (ST) [4,9,10] are commonly used as template materials for Pb-based perovskite ceramics. Numerous studies have demonstrated that textured materials such as PMN-PZT[11,12], BMT-PMN-PT[8], PNN-PZT[6,7], PYN-PMN-PT[13], 0.19PIN-0.445PSN-0.365PT[2], 0.7 mol% Mn-doped 0.675PMN-0.325PT[14], 0.36PIN-0.30PMN-0.34PT[15] ceramics, and PZT-PZNN thick films[16] exhibit superior properties when using BT templates. Additionally, ST templates show good applicability in systems like PMN-32.5PT[17,18], PMN-40PT[9], PMN-28PT[4]. However, an excess of heterogeneous templates as

View Article Online
DOI: 10.1039/D5DT01206F

impurities compared to the matrix grain can lead to a deterioration of properties. In contrast, $PbTiO_3$ (PT) has the same crystal structure and elemental composition as the Pb-based matrix powder, making it an ideal choice to avoid introducing new impurities into the system. As a result, PT templates have gained significant attention as a new template material.

Topochemical microcrystal conversion of the Aurivillius phase $PbBi_4Ti_4O_{15}$ in a $NaCl/Bi_2O_3/PbO$ flux system can yield various plate-shaped products. For instance, Yan[19] successfully prepared a PT template with minimal impurity phase at 1050 ℃ for 3 hours, which was then used to texture Sm-doped $PbTiO_3$ matrix powder. This resulted in a texture quality f of 95% and a piezoelectric voltage coefficient g_{33} value of 115×10^{-3} Vm/N. Similarly, Messing[20] synthesized lamellar $0.4(Na_{1/2}Bi_{1/2})TiO_3$-$0.6PbTiO_3$ (0.4NBT-0.6PT) at 1100 ℃ for 1 hour, which was utilized to texture PMN-PT and achieved a texture quality of 92% and a piezoelectric coefficient d_{33} value of 855 pC/N[21]. However, the reason for the different composition templates obtained under similar preparation conditions remains unclear. Additionally, attempts to synthesis plate-like PT templates with a size of 300-500 nm using the hydrothermal method were unsuccessful in meeting the requirements for TGG[22–24]. Furthermore, efforts to texture lead-based $0.83Pb(Zr_{1/2}Ti_{1/2})O_3$-$0.11Pb(Zn_{1/3}Nb_{2/3})O_3$-$0.06Pb(Ni_{1/3}Nb_{2/3})O_3$ (PZNNT) and $0.15PbZrO_3$-$0.3PbTiO_3$-$0.55Pb(Ni_{1/3}Nb_{2/3})O_3$ (PNN-PZT) using PT templates were also unsuccessful[25,26].

In order to assess the feasibility of using PT templates for textured lead-based piezoceramics, a comparative investigation was conducted on the microstructure,

View Article Online
DOI: 10.1039/D5DT01206F

electrical properties, and domain configuration of textured PMN-30PT ceramics with both BT and PT templates. PMN-30PT with a MPB composition, due to its excellent piezoelectric properties, was chosen as the host material[27–31]. In this study, we systematically investigated the texture developments, electric properties, and domain configurations of PMN-30PT ceramics with BT and PT templates. The results showed that achieving textured lead-based piezoceramics with PT templates is difficult. To further investigate the mechanism of texturing with PT templates, a comparative investigation was carried out on the differences between homogeneous PT templates and heterogeneous BT templates. This investigation included microstructures, morphologies, physical properties, topochemical microcrystal conversion, and the texture evolution process. Based on this comprehensive analysis, it was concluded that achieving textured piezoceramics with PT templates is a challenging task.

2. Experimental procedure

The PMN-30PT matrix powder was prepared using the traditional solid-state reaction method. Stoichiometric ratios of PbO, $Mg_2Nb_2O_6$, and TiO_2 were mixed, with an excess of 2 mol% PbO. The $Mg_2Nb_2O_6$ was pre-fabricated using $Mg_2(OH)_2CO_3$ and Nb_2O_5 to ensure a pure perovskite phase. The excess PbO compensates for evaporation. After 24 hours of ball-milling, the mixtures were calcined at 850 ℃ for 2 hours. The PMN-30PT matrix powder was then obtained by ball-milling again for 36 hours.

The plate-like <001> BT and PT microcrystals were synthesized using the topochemical microcrystal conversion method[19,32]. The BT template went through a

View Article Online
DOI: 10.1039/D5DT01206F

three-step synthesis process. First, $Bi_4Ti_3O_{12}$ was obtained by sintering Bi_2O_3 (99.0%; Sinopharm). and TiO_2 (99.5%; Alfa Aesar, China) in NaCl molten salts at 1100 ℃ for 5 hours. Then, the $Bi_4Ti_3O_{12}$ precursor was mixed with $BaCO_3$ (99.0%; Sigma Aldrich) and TiO_2 in $KCl/BaCl_2 \cdot 2H_2O$ (99.0%; Sinopharm) molten salts and calcined at 1080 ℃ for 2 hours to produce $BaBi_4Ti_4O_{15}$. Finally, the precursor $BaBi_4Ti_4O_{15}$ with excess $BaCO_3$ was held at 975 ℃ for 6 hours, resulting in the formation of the BT template and Bi_2O_3 byproduct. The PT template, on the other hand, underwent a two-step synthesis process. First, the $PbBi_4Ti_4O_{15}$ precursor was synthesized in molten salt. In the next step, the precursor was mixed with PbO and NaCl salt and heated to 1050 ℃ for 3 hours, yielding the PT template and Bi_2O_3 byproduct. All of the Bi_2O_3 byproduct was removed using diluted nitric acid (5wt%).

Textured ceramics were prepared by the cast tape slurry which consisted of ceramic matrix powder, 5wt% BT/PT templates, ethanol as solvent, polyvinyl butyral as binder, glycerol trioleate as dispersant, and polyethylene glycol as plasticizer. The 5wt% BT content has been determined through extensive literature[2,6,33] and self-conducted experiments, while the inclusion of 5wt% PT content serves as a point of comparison. The slurry was then cast at a rate of 40 cm/min using a doctor blade with a height of 200 μm. The dried tapes were cut into 10 mm×11 mm rectangles for stacking and lamination. Then the green samples slowly heated to 600 ℃ for 4 hours to remove the binder. They were then isostatically pressed at 200 MPa for 10 minutes. Afterwards, all of the samples were sintered at 800, 950, 1100 and 1250 ℃ for 2 hours.

The crystal structures were analyzed using powder X-ray diffraction (XRD;

View Article Online
DOI: 10.1039/D5DT01206F

D/max 2550 V, Rigaku, Japan). The XRD was performed using a Cu Kα1 ray source with a wavelength of 1.540 Å. The scanning angle ranged from 20° to 60° with a step size of 0.05°. Field-emission scanning electron microscopy (SEM; XL 30, Philips, Netherlands) was utilized to characterize the micro-morphology. The dielectric permittivity ε_r and dielectric loss $tan\delta$ were measured using an LCR meter (IM 3536, Hioki, Japan) with a temperature ranging from room temperature to 300 ℃. Hysteresis loop tests were conducted using a ferroelectric tester (TF Analyzer 2000, aixACCT, Germany) at a frequency of 1 Hz. The piezoelectric coefficient d_{33} was measured using a quasi-static d_{33}/d_{31} meter (ZJ-6A, Institute of Acoustics, China) after 15 minutes of poling at 2.5 kV/mm.

3. Results and discussion

3.1 PMN-30PT series ceramics

3.1.1. Crystal structure of PMN-30PT ceramics

View Article Online
DOI: 10.1039/D5DT01206F

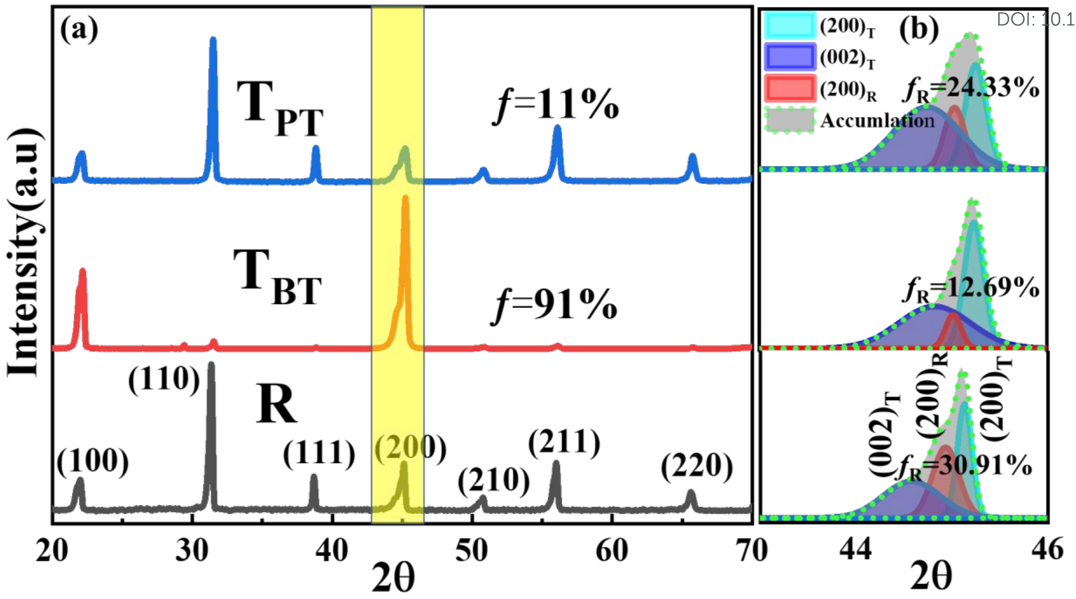

Fig. 1. (a) XRD patterns for random and textured PMN-30PT ceramics with BT/PT templates at room temperature; (b) corresponding expanded XRD patterns and peak-fitting in the range of 2θ from 43° to 46°.

Figure. 1(a) shows the XRD patterns of PMN-30PT ceramics for Random (R), textured with BT template (T_{BT}), and textured with PT template (T_{PT}). Both the random and textured PMN-30PT ceramics exhibited a pure perovskite structure. Based on the XRD results, the texture quality f values were calculated using the Lotgering equation : $f = (P - P_0)/(1 - P_0)$, where $\mathrm{P} = \sum \mathrm{I}_{(00l)}/\sum \mathrm{I}_{(hkl)}$, $\mathrm{P}_0 = \sum \mathrm{I}_{0(00l)}/\sum \mathrm{I}_{0(hkl)}$, $\sum \mathrm{I}$ and $\sum \mathrm{I}_0$ are the sums of the peak intensities of the XRD patterns for the textured and random ceramics, respectively. The texture of the ceramics was evaluated through the texture quality f for the (00l) direction (f_{00l}), with higher f_{00l} values indicating better orientation and better piezoelectric properties[9,34]. In this study, the f_{00l} values were determined to be 11% for T_{PT} and 91% for T_{BT}.

Figure. 1(b) exhibits the expanded XRD patterns and peak-fitting in the range of 2θ from 43° to 46°, corresponding to the (200) direction. Notably, there is a clear split

View Article Online
DOI: 10.1039/D5DT01206F

in the peak at approximately 45°, indicating the coexistence of rhombohedral and tetragonal phases in the samples. By fitting the peaks in this region using Lorentzian-Gaussian functions, the peak can be deconvoluted into three peaks: $(002)_T$, $(002)_R$, and $(200)_T$. The subscripts “T” and “R” denote the tetragonal and rhombohedral phases, respectively. The fraction of the rhombohedral phase (f_R) can be determined by integrating the peak intensities of the two phases (I_T and I_R) using the equation: $f_R = I_R / (I_T + I_R) = I(002)_R / [I(002)_T + I(200)_T + I(002)_R]$. It was observed that the fraction of the rhombohedral phase was lower in the textured ceramics compared to the random ceramic. This phenomenon can be attributed to the fact that the doped BT and PT templates are tetragonal at room temperature.

3.1.2. Morphologies and EDS images of PMN-30PT Textured ceramics evolution process

View Article Online
DOI: 10.1039/D5DT01206F

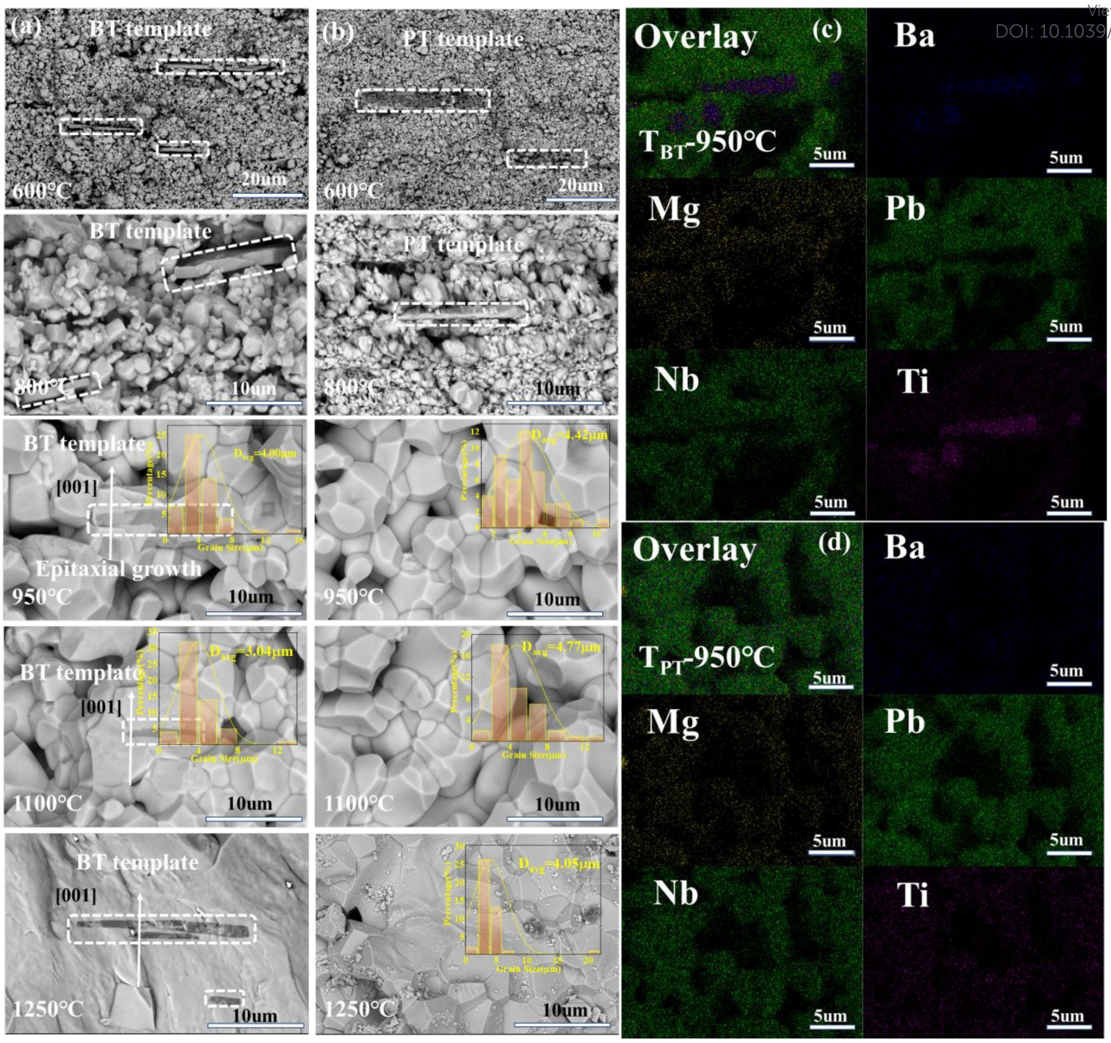

Fig. 2. SEM images of the fracture morphology and grain size distribution charts in T_{BT} (a) and T_{PT} (b) ceramics sintered at different temperature for 2 hours. EDS images of each element in T_{BT} (c) and T_{PT} (d) ceramics sintered at 950℃.

Figures. 2(a-b) show scanning electron microscopy (SEM) images and grain size distribution charts for T_{BT} and T_{PT} ceramics. To further quantify the grain size and preferred orientation, we investigated the texture development during the sintering process at temperatures of 600-800-950-1100-1250 °C. At 600 °C, the BT templates were uniformly dispersed in the matrix powder, while the PT templates were poorly dispersed, with larger and thicker templates and unclear edges. At 950 °C, both T_{BT}

and T_{PT} samples began to porcelainize and further densify at subsequent temperatures. The T_{BT} sample exhibited epitaxial growth with a selective orientation and an increase in texture quality, while there was no selective orientation for T_{PT}. It is important to note that the T_{BT} grain sizes underwent significant changes as the temperature increased, eventually forming a large "brick-wall" structure grain due to epitaxial growth. Figures. 2(c-d) show the EDS images of T_{BT} and T_{PT} at 950 °C. It is clear that T_{BT} exhibits a distinct distribution of the BT template, with a significantly higher Ti content compared to the matrix powder. On the other hand, the presence of the PT template in T_{PT} is not easily discernible, indicating that the PT template readily fuses with the matrix powder, resulting in the formation of a homogeneous ceramic material. At 1250 °C, the fracture microstructure of the sintered sample was examined. This specific temperature and duration have been found to strike a balance between achieving high densities and texture quality in the ceramics[2,13,33,35]. The textured ceramics exhibited distinct, isolated brick-like structures with BT templates, measuring 4-10 μm in length and 0.5-1 μm in thickness. The matrix powder underwent epitaxial growth on the BT templates, causing the BT template to be positioned within the matrix powder as an impurity. On the other hand, the grain size changes in T_{PT} were not as significant, with an average size of 4 μm. The grain at 950 °C follows a more consistent normal distribution. As the temperature reached 1250 °C, there were a large number of small grains surrounding a large grain with a random orientation structure. T_{PT} did not exhibit a brick-like structure, and the PT template was not discernible in the final product.

View Article Online
DOI: 10.1039/D5DT01206F

3.1.3. Dielectric, ferroelectric and piezoelectric properties of PMN-30PT series ceramics

As depicted in Figures. 3(a)–(c), each sample exhibited noticeable peak broadening and frequency dispersion, indicating relaxation characteristics. The difference in T_m at frequency of 1 kHz and 100 kHz, represented by ΔT, is a measure of the strength of frequency dispersion, with a larger ΔT indicating stronger dispersion. The textured ceramics displayed a higher degree of broadening in the dielectric peak compared to the random ceramic. The T_{BT} sample exhibited the highest ΔT (4 ℃), suggesting that the presence of the BT template has a significantly impact on the dielectric peak. The BT template in the textured ceramics has a core-shell structure resulting in inhomogeneous chemical properties. This contributes to the plateau near the dielectric peak, ultimately enhancing the relaxation behavior[37]. Figure. 3(d) displays the changes in dielectric constant (ε_r) and dielectric loss ($tan\delta$) at 1 kHz. The textured ceramics exhibit a lower dielectric constant compared to random ceramic. The addition of the template results in a decrease in room temperature relative permittivity (ε_r). This is because the BT (ε_r, 1400) and PT (ε_r, 142) templates have a low dielectric constant, causing the overall dielectric constant of the textured ceramics to decrease with an increase in BT content. According to the brick-wall model, the total capacitance of the textured ceramics is equivalent to the series and parallel connections of the matrix and fillers[38]. This means that the dielectric permittivity of the 0-3 composite structure with matrix grains and templates is lower than that of PMN-30PT. Interestingly, T_{PT} has a higher dielectric constant than T_{BT}, indicating that T_{PT} does not

View Article Online
DOI: 10.1039/D5DT01206F

have a "brick-wall" structure.

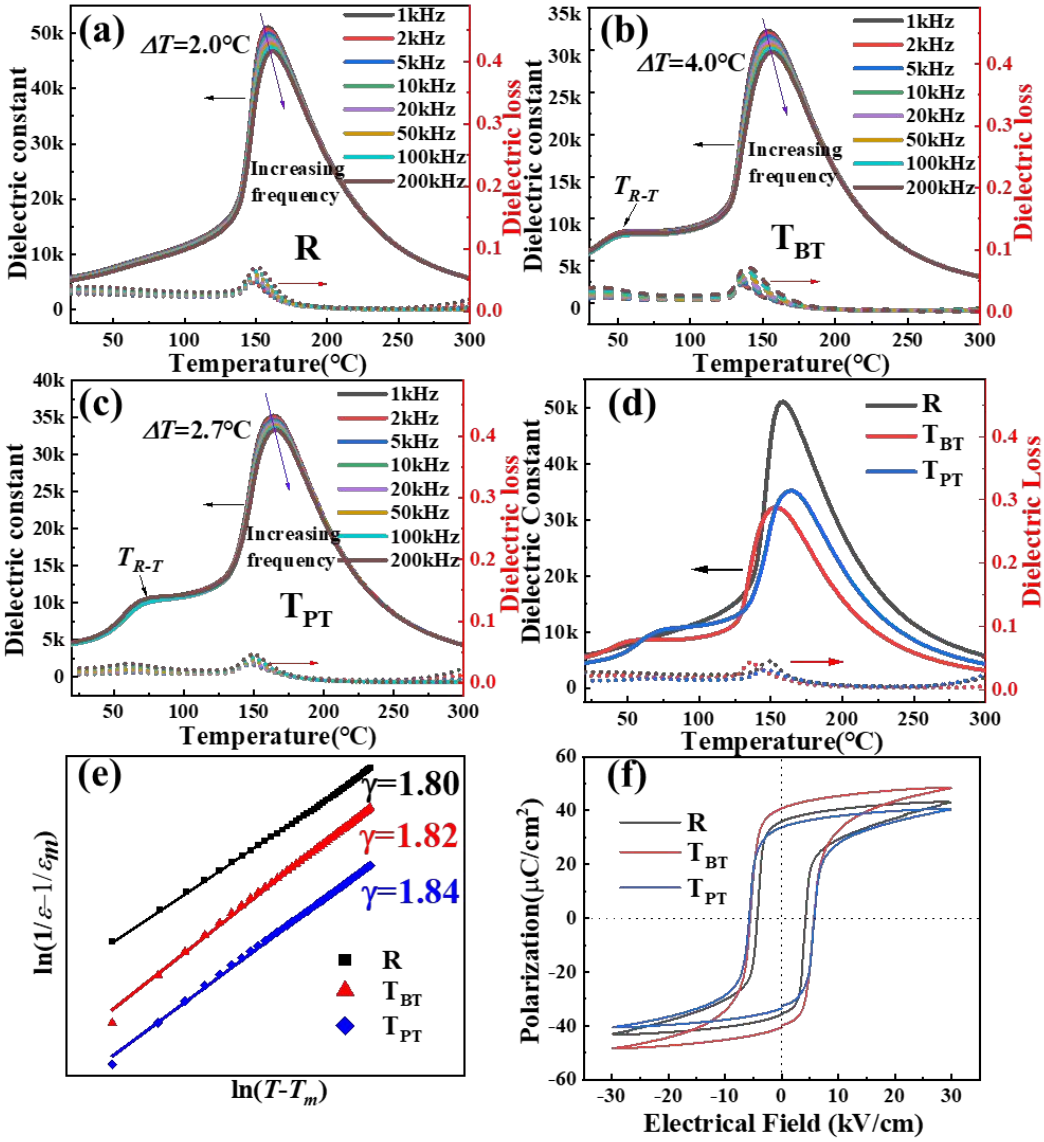

Fig. 3. The dielectric constant (ε_r) and loss ($tan\delta$) as a function of temperature: (a) Random ceramic, (b) Textured ceramics with 5wt% BT templates, (c) Textured ceramics with 5wt% PT templates, and Comparison of samples at 1 kHz (d) ε_r and $tan\delta$, (e) the function of $\ln(1/\varepsilon_r - 1/\varepsilon_m)$ with respect to $\ln(T - T_m)$, (f) $P-E$ hysteresis loops of PMN-30PT ceramics at 30 kV/cm with a frequency of 1 Hz.

The dielectric relaxation behavior of PMN-30PT ceramics was investigated using the modified Curie–Weiss law: $1/\varepsilon_r - 1/\varepsilon_m = (T-T_m)^{\gamma}/ C$, where γ represents the

View Article Online
DOI: 10.1039/D5DT01206F

diffusion coefficient (γ is 1 for normal ferroelectric and 2 for perfect relaxor ferroelectrics) and C is a constant. The calculated data points were linearly fitted to determine the value of γ, corresponding to the slope of the line. The relationship between $\ln(1/\varepsilon_r – 1/\varepsilon_m)$ and $\ln(T – T_m)$ is illustrated in Figure. 3(e). It is evident that the γ values for both random and textured ceramics fall within the range of 1.80 to 1.84. The observation indicated that all samples exhibit significant diffuse phase transition (DPT) behavior and are close to ideal relaxor ferroelectrics. Compared to random ceramic, textured ceramics exhibit higher relaxation behavior. In particular, T_{BT} sample demonstrate a maximum diffusion coefficient (γ) of 1.84. The reason may be due to the effect of interfacial strain between the matrix and the template, similar to the pressure-induced dielectric relaxation behavior calculated by First-principles calculation and observed in PZN-PT[39,40].

Figure. 3(f) displays the $P-E$ hysteresis loops of PMN-30PT ceramics at 30 kV/cm. All loops demonstrate excellent saturation hysteresis. Sample R has a coercive field (E_c) of 4.2 kV/cm, while the textured sample exhibits a higher E_c of 5.7-5.8 kV/cm, indicating a “hard” characteristic. This can be attributed to the interfacial strain caused by the lattice mismatch between the PMN-30PT matrix grain and the template grain in the textured ceramics. The strain act as a clamping effect, hindering domain wall motion and making polarization switching more challenging[41]. The residual polarization (P_r) decreases from 35.9 μC/cm^2 for the R sample to 33.8 μC/cm^2 for the T_{BT} sample. This decrease is attributed to the increase in textured grains aligned along the [00*l*] orientation[42], which have lower P_r values. However, T_{PT}

DOI: 10.1039/D5DT01206F

sample shows an increase in P_r up to 40.8 μC/cm^2. This is because the PT template has a lower orientation and increases the number of grain boundaries, thereby enhancing the P_r values. It is worth noting that the piezoelectric coefficients of 840 pC/N for T_{BT} sample and 534 pC/N for T_{PT} sample are much higher than that of 489 pC/N for random ceramics, and the specific results are shown in Table. 1.

Table. 1. The dielectric, ferroelectric and piezoelectric properties of PMN-30PT ceramics.

Sample	Random	T_{BT}	T_{PT}
d_{33} (pC/N)	489	824	534
T_{R-T} (℃)	-	53	75
T_m (℃)	159	153	164
ε_m (T_m)	51.1k	32.6k	35.1k
P_{max} (μC/cm^2)	46.1	40.4	43.1
P_r (μC/cm^2)	35.9	33.8	40.8
E_c (kV/cm)	4.20	5.79	5.69
Tanδ	4.51%	4.26%	3.11%

3.1.4. Domain configuration of PMN-30PT series ceramics

The piezoelectric properties of relaxor ferroelectric materials are significantly affected by their domain morphology. Previous research has shown that in order to achieve superior piezoelectric characteristics, the domain size should be smaller or the domain wall density should be higher[41,43–46]. A simple and effective method for studying the local domain morphology of ferroelectric single crystals and ceramics is through the use of piezoelectric force microscopy (PFM)[47,48]. PFM is able to directly

DOI: 10.1039/D5DT01206F

observe the domain structure evolution of ferroelectric materials under the applied electric field, which provides an important experimental means to study the microstructure and properties of ferroelectric materials[49]. In order to explore the microscopic domain structure of the textured PMN-30PT ceramics, the domain configurations of the T_{BT} and T_{PT} samples were investigated using PFM. The out-of-plane PFM amplitude and phase patterns are exhibited in Figures. 4(a-d), respectively. The PFM image clearly shows the reduction in domain size due to a higher texture quality f value from Figures. 4(a) and (c). Phase and amplitude patterns represent the direction and the size of polarization, respectively. The small domain size (high domain wall density) could improve the extrinsic contributions and facilitate the nucleation and growth of evolved domains[50]. Therefore, our results are consistent with the fundamental principle of domain dynamics[51], indicating that the smaller sized domain structure is essential for the excellent piezoelectric and electromechanical coupling properties of T_{BT} sample compared to the T_{PT} sample.

View Article Online
DOI: 10.1039/D5DT01206F

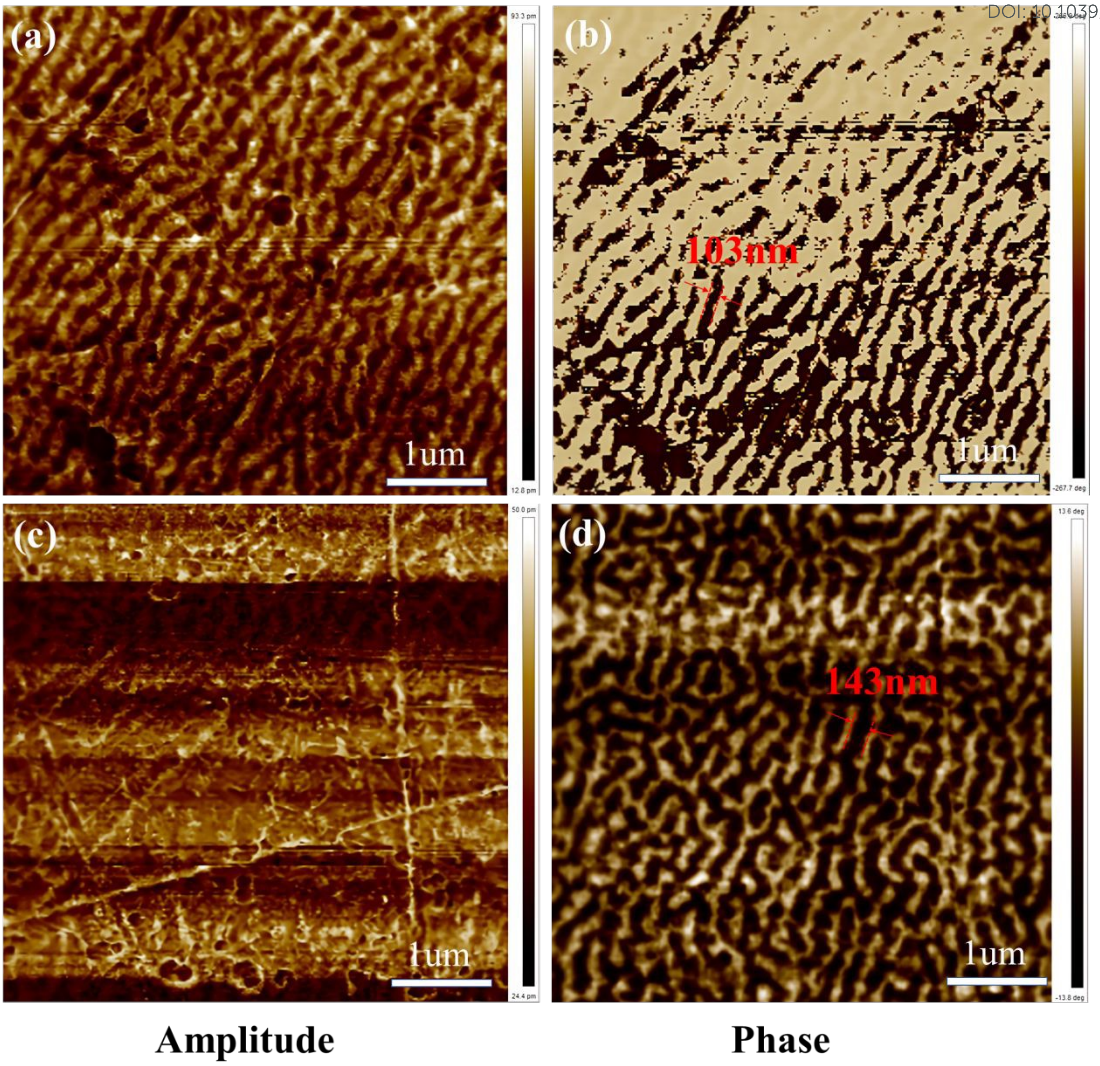

Fig. 4. The PFM out-of-plane images of PMN-30PT textured ceramics at room temperature: (a) amplitude image and (b) phase image of T_{BT}; (c) amplitude image and (d) phase image of T_{PT}.

A shift in polarization direction is indicated by a change in the lining of PFM phase patterns[52,53]. A darker lining signifies a larger change in polarization direction, making it easier to visualize the ferroelectric domain structure of the sample. In randomly oriented ceramics, the regular domain patterns are only present in individual grains, while the overall ceramic does not exhibit a well-arranged domain structure. However, in textured ceramics with the larger grain size and a fixed orientation of the [001]

View Article Online
DOI: 10.1039/D5DT01206F

crystallographic axis within the grains at a high Lotgering factor, a striped domain pattern similar to that separated by the 109° domain wall is formed. It should be noted that this condition is relaxed for the other two axes, which have randomly distributed orientations. As a result, there are electrical and elastic correlations between neighboring grains that cannot be ignored. These correlations drive the formation of stripe-like domain patterns with non-109° domain walls. These stripe-like domain structures are not observed in randomly oriented polycrystalline ceramics[54–56]. In the T_{BT} sample, the domain structure is dominated by parallel striped domains (Figure. 4(b)), indicating a polarization direction towards to the same direction. In contrast, the T_{PT} sample with a lower $[001]_c$ texture quality shows an ordered fingerprint-like pattern dominating the domain structure (Figure. 4(d)). Eventually, the textured ceramics T_{BT} show a much smaller domain size (103 nm) compared to the random oriented ceramic T_{PT} (143 nm). This smaller domain size greatly increases the domain wall density and enhances the extrinsic contributions of the piezoelectric response[57]. Compared to the fingerprint-like domain structure, the domain switching in the parallel striped domain structure is more sensitive to the applied electric field and induces a larger strain. As a result, it has a significant effect on the piezoelectric properties of the ceramics.

In conclusion, texture engineering has been shown to significantly improve the piezoelectric properties of PMN-30PT ceramics. To highlight the significance of this work, we have presented the piezoelectric coefficient and texture quality of lead-based piezoceramics, as illustrated in Figure. 5. By comparing random piezoceramics with their textured counterparts, we have analyzed the increased rate in the piezoelectric

View Article Online
DOI: 10.1039/D5DT01206F

coefficient. It is worth noting that the 5wt% PT templates were uniformly dispersed in the PMN-30PT matrix ceramic, resulting in a PMN-32.5PT ceramic through calculation. However, the piezoelectric coefficient d_{33} of this ceramic is only 450 pC/N[58], which is lower than the value achieved in our work of T_{PT} ceramic (534 pC/N). Additionally, as shown in Figure. 5, our textured ceramic T_{BT} has the highest increased rate in piezoelectric coefficient, which is significantly greater than the increased rate observed in other ternary lead-based ceramics.

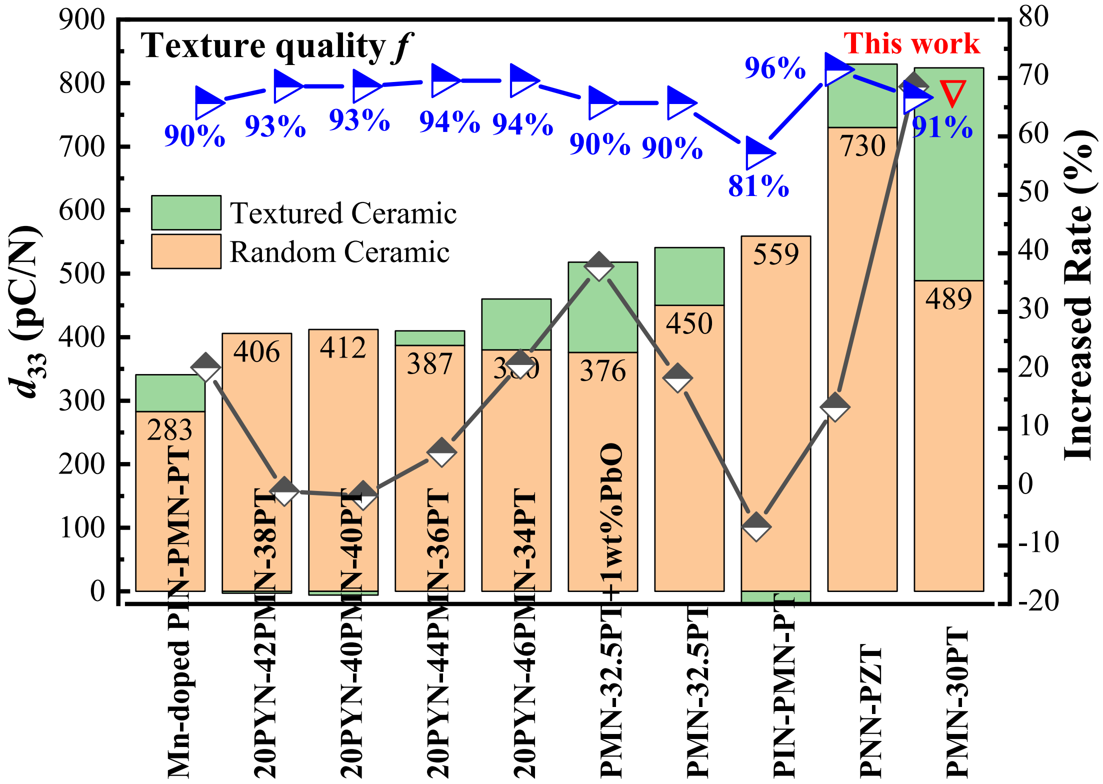

Fig. 5. The piezoelectric constants d_{33}, increased rate, and texture quality *f* of random ceramics and corresponding textured ceramics in PIN-PMN-PT[35], PYN-PMN-PT[13], PMN-32.5PT[58], and PNN-PZT[7].

3.2. BT and PT templates

View Article Online
DOI: 10.1039/D5DT01206F

3.2.1 Structure and micromorphology of BT and PT templates

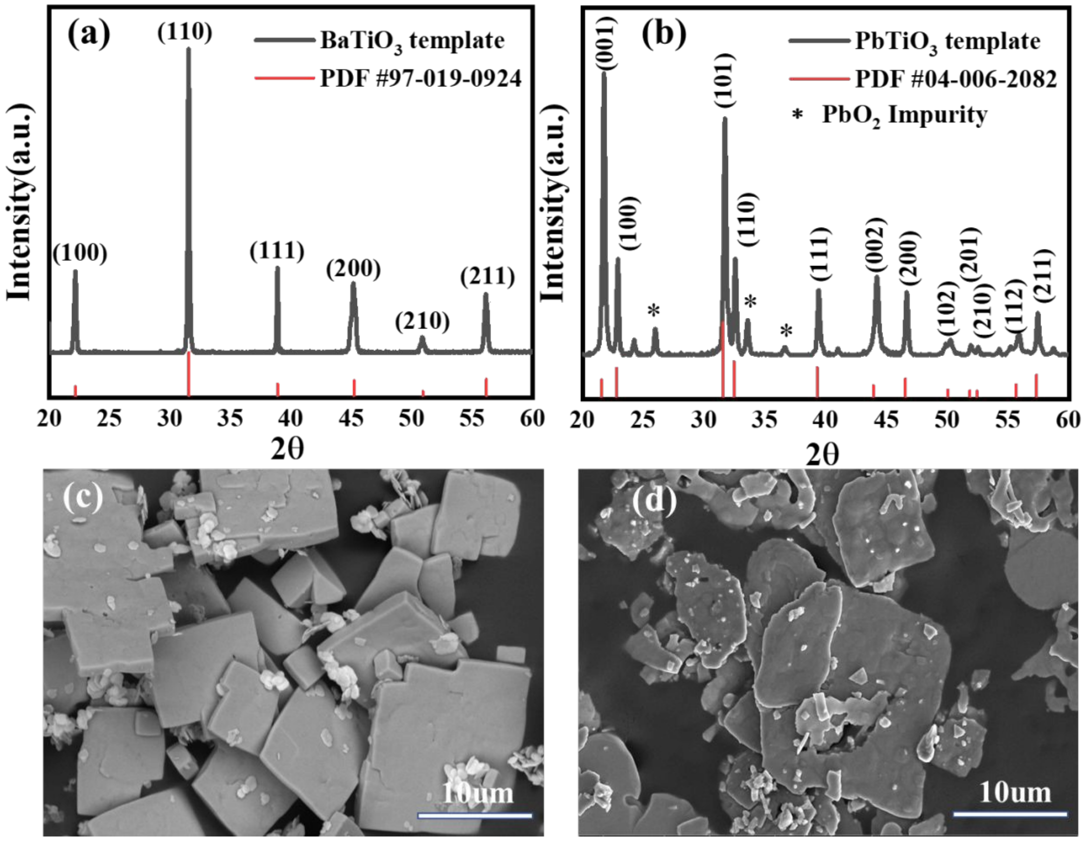

Fig. 6. XRD patterns of BT (a) and PT (b) template; Micromorphology of BT (c) and PT (d) template.

Figures. 6(a-d) show the XRD patterns and morphology of the BT and PT templates incorporated into the PMN-30PT textured ceramics. The XRD patterns of the BT templates indicate a high level of purity, as exhibited in the comparison with the standard powder diffraction file (PDF) for the BT template in Figure. 6(a). The SEM image in Figure. 6(c) also supports this characteristic, showing sharp and non-bonded edges, and a more homogeneous morphology for the BT templates. In contrast, Figure. 6(b) compares the formed PT templates with the standard PDF card. It is evident that a significant amount of PT template has formed, with a selective

View Article Online
DOI: 10.1039/D5DT01206F

orientation in the (00*l*) direction. This characteristic suggests that the PT templates were originally formed extremely large sheet products, resulting in a distinct selective orientation. And the presence of hetero-phase PbO_2 also suggests an abundance of Pb^{2+} in the PT template. It is worth noting that excessive PbO_2 impurity in the templates can lead to excessive substitution of Bi^{3+} in the Aurivillius templates, which can lead to the destruction of the Bi_2O_2 layer structure, thus leading to the disappearance of the lamellar morphology. Additionally, the SEM image in Figure. 6(d) reveals that the PT templates are bonded in large pieces, lacking sharp edges, and exhibiting an inhomogeneous and hollow surface. This contributes to their low thermal stability, likely due to the large flaky PT templates originating from the melting of PbO, which bonds them together.

3.2.2. Topochemical microcrystal conversion in BT and PT template preparations

To compare the preparation processes of BT and PT templates, we eliminated the heat preservation step and increased the heating rate. This ensured that the template reaction process remained incomplete, preserving the morphologies at each stage. Figures. 7(a) and (c) illustrate that the BT template generation process resulted in sharper templates with a flaky morphology. This is due to the insufficient heat preservation time, resulting in templates of varying sizes and shapes. The thickness of these templates is approximately 150 nm, with a large diameter to thickness ratio. On the other hand, the PT template formed a more uniform single-layer sheet-like structure with non-sharp edges (Figure. 7(b)). The detailed morphology of the flower-like nanostructure is shown in Figure. 7(d) as a magnified SEM image, illustrating that the entire 3D flower-like $PbTiO_3$ nanostructure is self-assembled by nanosheets with a smooth surface. Each layer of the sheet has a thickness of approximately 20 nm, and there is some disordered bonding between the nanosheets, similar to the PT templates synthesized by hydrothermal treatment[22,24]. To analyze the reasons for the inconsistent morphology of the two templates, we investigated the topochemical microcrystal conversion of BT and PT.

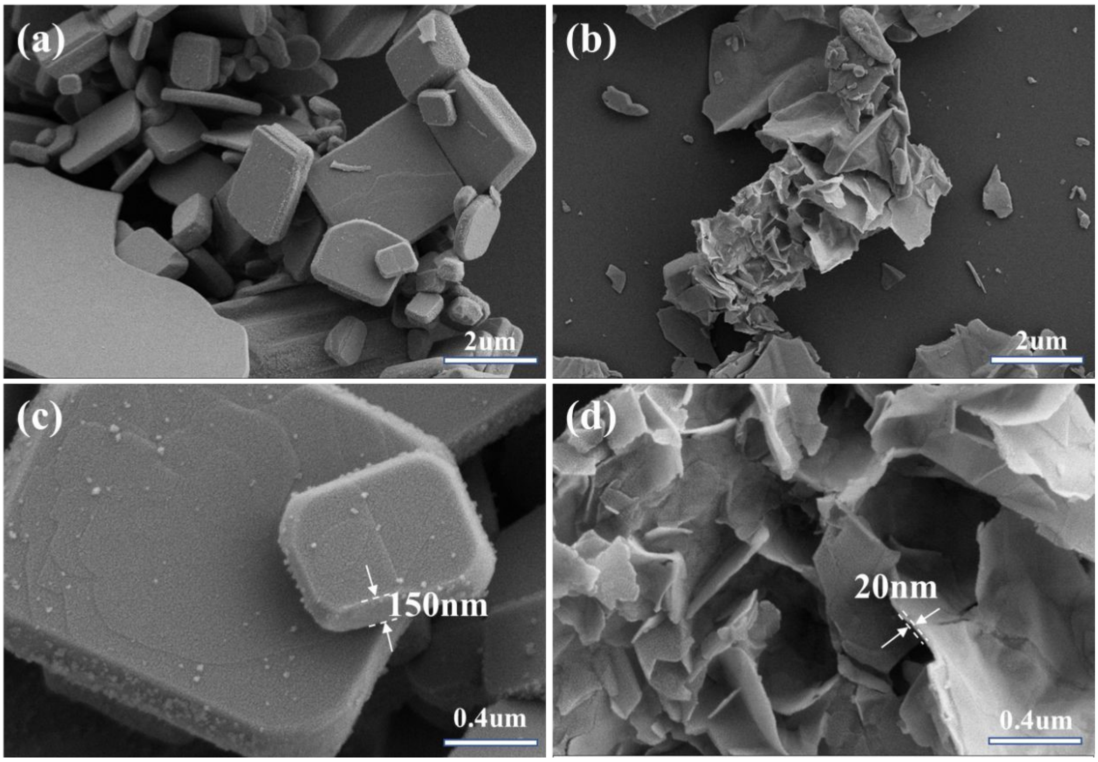

Fig. 7. Micromorphology of BT template (a) and PT template (b); zoomed-in areas of BT template (c) and PT template (d) after eliminating the heat preservation step and increasing the heating rate.

The relevant chemical reaction formulae are given below:

$$BaBi_4Ti_4O_{15} + 3BaCO_3 = 4BaTiO_3 + 2Bi_2O_3 + 3CO_2 \quad (1)$$

$$PbBi_4Ti_4O_{15} + 3PbO = 4PbTiO_3 + 2Bi_2O_3 \quad (2)$$

Based on the presented formulae and SEM results, it can be inferred that BT precipitated from $BaBi_4Ti_4O_{15}$ (BBIT) formed varying-sized morphologies and underwent an *Ostwald* ripening process. On the other hand, PT precipitated from $PbBi_4Ti_4O_{15}$ (PBIT) formed interlayer exfoliation, followed by melt-bonding with PbO at high temperatures. The bulk PT nanosheet retains the (00*l*) orientation, which is maintained even after melt bonding. To further analyze the topochemical microcrystal conversion of the two templates, we attempted to combine the topochemical conversion process with the associated crystallographic information file (CIF). Figures. 8(a) and (c) illustrates the topochemical conversion process of the BBIT/PBIT precursor into BT/PT. It can be observed that the conversion process is nearly identical. During the conversion process, the *A*-site cation displaces the Bi^{3+} cation and forms the final template. To analyze the differences in the topochemical conversion processes of BT and PT, we examined the differences in the site occupancy factor (SOF) during the conversion of their precursors PBIT and BBIT. We standardized the atomic occupancies of the cations in the structures and found that the Ti^{4+} cations are positioned at the *B*-site of the TiO_6 octahedron with the same occupancies. The Pb^{2+} and Ba^{2+} cations are both located at the *A*-site with Bi^{3+}, as shown in Figure. 8(b), where Bi (1) represents the Bi layer position, and the numbers 1, 2, and 3 represent the position of a different Bi layer. In terms of the topochemical conversion process, the two conversion processes are identical, and theoretically, there should not be a formation of two SEM images with different shapes. To further understand the differences between BT and PT in the conversion process, we

View Article Online
DOI: 10.1039/D5DT01206F

reviewed the CIF files of BBIT and PBIT and tabulated the differences.

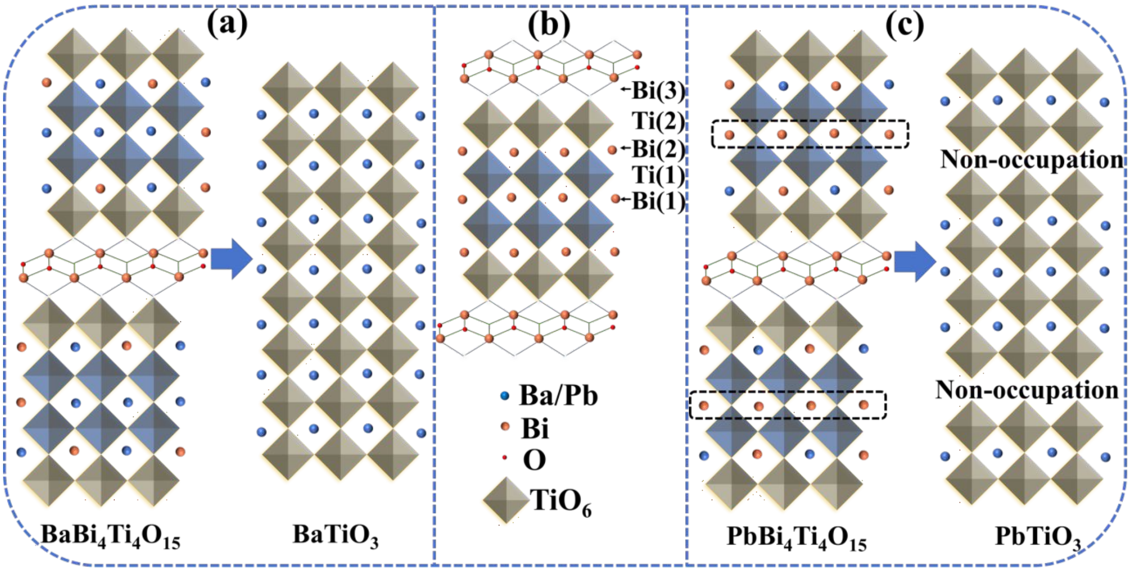

Fig. 8. Schematic illustration of topochemical microcrystal conversion (a) from $BaBi_4Ti_4O_{15}$ to $BaTiO_3$, (c) from $PbBi_4Ti_4O_{15}$ to $PbTiO_3$. (b) Representation of the structure of the n = 4 Aurivillius oxides $ABi_4Ti_4O_{15}$.

3.2.3. The occupancy of Pb^{2+} and Ba^{2+} in the Aurivillius phase of precursors in BT and PT templates

Table. 2 illustrates the refined structure parameters of Aurivillius phase of $ABi_4Ti_4O_{15}$ and the corresponding occupancy of Pb^{2+} and Ba^{2+} in each layer. The Bi_2O_2 layer contains *A*-type cations (Pb^{2+}, Ba^{2+}), and the number of cations in this layer depends on their *Shannon* radius. The *Shannon* radius of Ba^{2+} is 1.61 Å, which is larger than the radius of Pb^{2+} (1.49 Å), resulting in a percentage increase of site occupancy factor (SOF) from 28% in BBIT to 41% in PBIT[59]. Notably, Pb^{2+} is absent at the 4a position, indicating its difficulty in existing there[59,60]. This can be attributed to the fact that Pb^{2+} and Bi^{3+} have $6s^2$ lone-pair electron configurations, this disorder

View Article Online
DOI: 10.1039/D5DT01206F

between Pb^{2+} and Bi^{3+} has been observed in $PbBi_2Nb_2O_9$[61,62]. The substitution of Bi^{3+} with Pb^{2+} leads to chaotic substitution and interlayer detachment at the 4a position, resulting in the formation of PT nanosheets. Furthermore, the origin of ferroelectric behavior in $PbTiO_3$ differs from that of $BaTiO_3$. In $PbTiO_3$, the hybridization of Pb^{2+} *6s* electron orbitals with oxygen *2p* electron orbitals creates a more covalent Pb-O bond, which stresses the oxygen octahedra and stabilizes the ferroelectric phase. On the other hand, in $BaTiO_3$, the hybridization of Ba^{2+} *5p* electron orbitals does not occur with the valence band[63]. This ultimately leads to the formation of Ba-O ionic bonds, which require lower activation energy than Pb-O covalent bonds. This is particularly evident at the 4a position, where there is no pre-existing Pb-O bond. As a result, a higher activation energy is needed for the re-formation of the Pb-O bond, making it difficult to form a Pb-O bond at the 4a position. This leads to fracture and the formation of PT nanosheets. This also explains why the conversion of PBIT to PT (1080 ℃) requires a higher preparation temperature than the conversion of BBIT to BT (975 ℃).

Table. 2. Refined structure parameters of Aurivillius phase of $ABi_4Ti_4O_{15}$ (A= Pb, Ba)

Atom	Site	SOF[59]	
		Ba	Pb
Bi (1)	4a	0.8	0
Bi (2)	8b	0.31	0.66
Bi (3)*	8b	0.28	0.41
Ti (1)	8b	1	1

Ti (2)	8b	1	1

View Article Online
DOI: 10.1039/D5DT01206F

According to the location of the Bi layers, it can be seen that Pb^{2+} only exchanges with Bi^{3+} ions in the 8b layers, while the Bi^{3+} ions in the 4a layer cannot be exchanged. In order to verify this inference, we re-grew the PT template in the molten salt NaCl and KCl system. It was found that the PT template re-grew into a thick, sharp template. XRD analysis revealed that the composition of this template was $Pb_3Bi_4Ti_6O_{21}$ (Figures. 9(a-b)). This indicates that the prepared PT templates still contain a large amount of Bi element. However, the XRD tests on the PT templates (Figure. 6(b)) did not detect the presence of Bi. This suggests that Bi element is present in the inner structure of the PT template, in the form of PBIT, while the surface remains porous due to the use of diluted nitric acid. Therefore, it is not possible to completely remove the Bi^{3+} ions while maintaining the lamellar morphology. Interestingly, two lead titanates and one former unreacted PBIT prepared in the molten salt NaCl and KCl system formed exactly $Pb_3Bi_4Ti_6O_{21}$. The reaction equation is $PbBi_4Ti_4O_{15} + 2PbTiO_3 = Pb_3Bi_4Ti_6O_{21}$, and the schematic illustration of topochemical microcrystal conversion from $PbBi_4Ti_4O_{15}$ and $PbTiO_3$ to $Pb_3Bi_4Ti_6O_{21}$ was shown in Figure. 9(c). It is worth noting that the Pb-based Aurivillius ceramics $Pb_xBi_4Ti_{3+x}O_{12+3x}$ have various compositions, including $x = 0$ ($Bi_3Ti_4O_{12}$, BIT)[64], $x = 1$ ($PbBi_4Ti_4O_{15}$, PBIT)[60] and $x = 2$ ($Pb_2Bi_4Ti_5O_{18}$, P_2BIT)[65], $x = 3$ ($Pb_3Bi_4Ti_6O_{21}$, P_3BIT)[66–68], and $x = 4$ ($Pb_4Bi_4Ti_7O_{24}$, P_4BIT)[68]. This implies the substitution between Pb^{2+} and Bi^{3+} is disordered, making it difficult to completely replace the Bi^{3+} ions

View Article Online
DOI: 10.1039/D5DT01206F

using the topochemical conversion method. However, in the Aurivillius ceramic $Ba_xBi_4Ti_{3+x}O_{12+3x}$, there is a directional substitution of Ba^{2+} for Bi^{3+}, which only occurs for $x = 0$ ($Bi_3Ti_4O_{12}$, BIT)[64], $x = 1$ ($BaBi_4Ti_4O_{15}$)[60,69], and $x = 2$ ($Ba_2Bi_4Ti_5O_{18}$)[65].

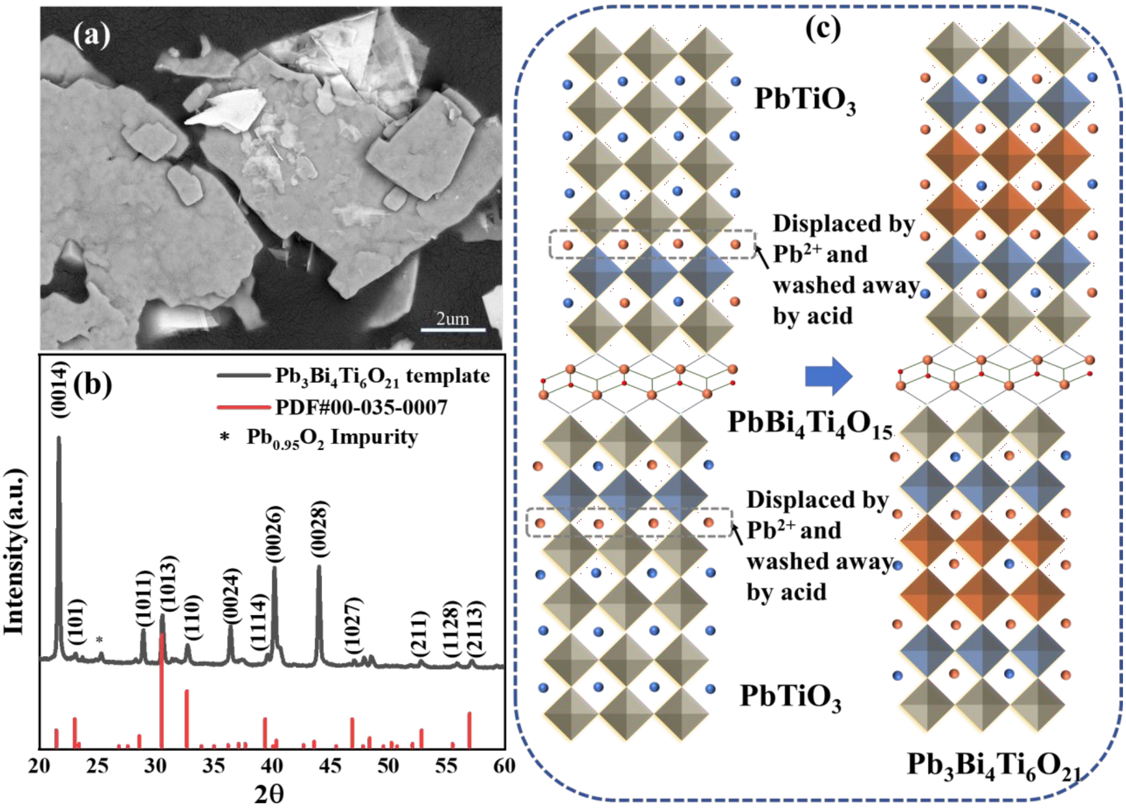

Fig. 9. Morphology (a), XRD pattern (b), and Schematic illustration (c) of topochemical microcrystal conversion from $PbBi_4Ti_4O_{15}$ and $PbTiO_3$ to $Pb_3Bi_4Ti_6O_{21}$.

3.2.4. Preparation of Pb-based Aurivillius $Pb_xBi_4Ti_{3+x}O_{12+3x}$ (x=1, 2, 3, 4) templates

Since the substitution of Pb^{2+} and Bi^{3+} is disordered, it is difficult to completely displace Bi^{3+} using the topochemical conversion method. Therefore, we attempted to further explore the use of Pb-based Aurivillius precursors and analyze the evolution of residual Bi^{3+} in the matrix ceramics. To achieve this, we synthesized $Pb_xBi_4Ti_{3+x}O_{12+3x}$

View Article Online
DOI: 10.1039/D5DT01206F

(x = 1,2,3,4) precursors by referring to the method of PT template preparation with the following equations:

$$xPbO + 2Bi_2O_3 + (x + 3)\ TiO_2 = Pb_xBi_4Ti_{3+x}O_{12+3x} \qquad (3)$$

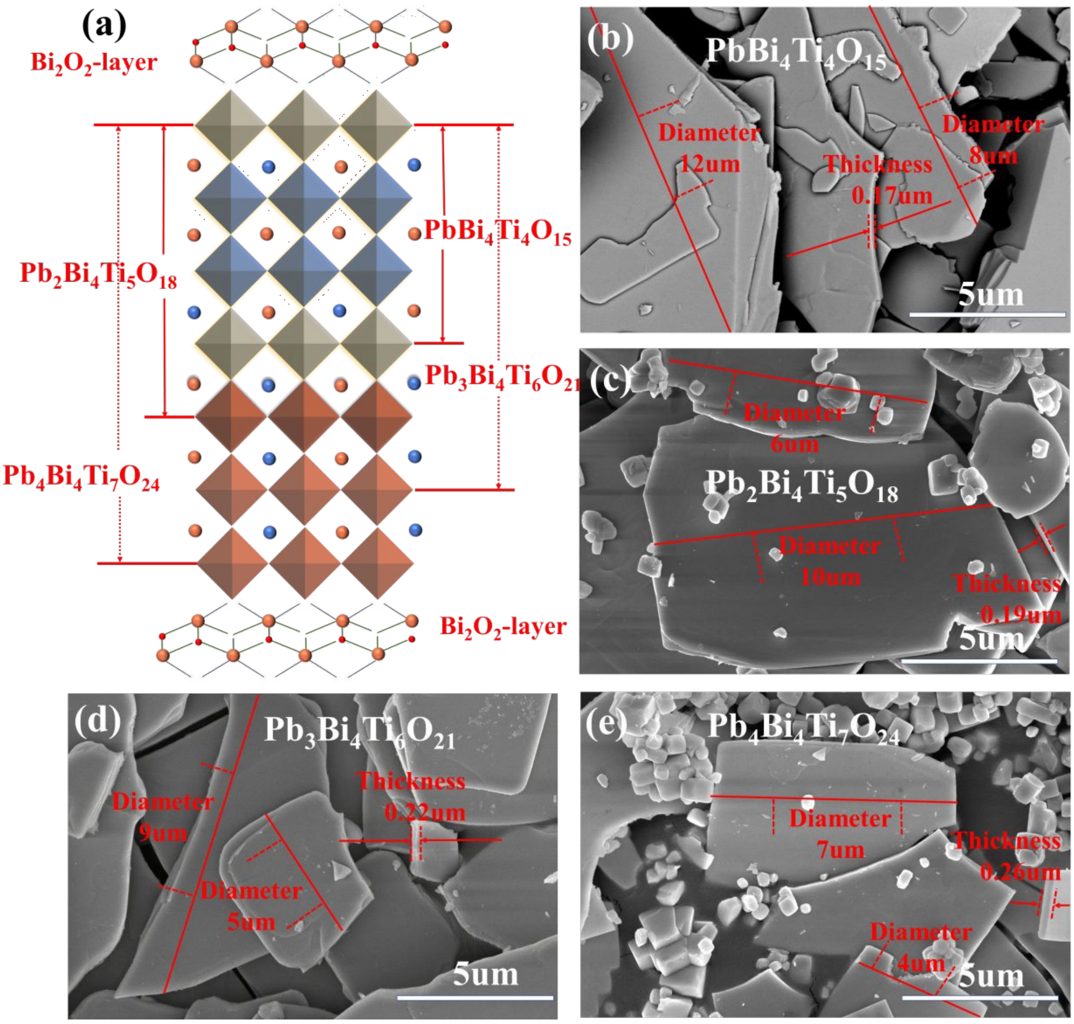

Fig. 10. Schematic illustration (a) and Morphologies (b-d) of Pb-based Aurivillius $Pb_xBi_4Ti_{3+x}O_{12+3x}$ (x = 1, 2, 3, 4) templates.

Figure. 10 (a) illustrates a schematic representation of the structure with different layers of TiO_6 octahedra in Pb-based Aurivillius templates, where $PbTiO_3$ is embedded in the Aurivillius structure to increase the number of TiO_6 octahedral layers. This means that when Bi^{3+} is present in the matrix ceramics, $Pb_xBi_4Ti_{3+x}O_{12+3x}$ is inevitably formed, while the number of TiO_6 octahedral layers increases with the $PbTiO_3$-rich matrix and templates. The morphologies of Pb-based Aurivillius templates are further demonstrated in Figures. 10(b-d). As the number of TiO_6 octahedral layers increases, the thickness of the templates also increases from 0.17 μm (x=1) to 0.26 μm (x=4), while the diameter decreases from 8-12 μm (x=1) to 4-7 μm (x=4). This ultimately leads to a decrease in the diameter-to-thickness ratio. Additionally, since the texture process requires the template to have similar lattice parameters as the matrix powder, this can facilitate the epitaxial growth of the matrix powder along the template. Table. 3 compares the lattice parameters and morphology parameters of the matrix powder and $Pb_xBi_4Ti_{3+x}O_{12+3x}$ templates, revealing that the difference in a-axis lattice parameters between the templates and matrix powder is more than 35%. This large lattice mismatch fundamentally results in no epitaxial growth, and further explains how Bi affects the ceramic texture evolution.

Table. 3. The Lattice parameters and Morphologies of $Pb_xBi_4Ti_{3+x}O_{12+3x}$ (x=1,2,3,4) templates.

Ceramics Composition	**Lattice parameters**						**Morphologies**	
	Space group	a(Å)	b(Å)	c(Å)	c/a	△a/a (%)	Diameter (μm)	Thickness (μm)
PMN-30PT	P4mm	4.00	4.00	4.05	1.01	-	0.2	0.2
PBIT template[59]	$A2_1am$	5.45	5.43	41.4	7.60	36.3	8-12	0.17
P_2BIT template[65]	$A2_1am$	5.47	5.46	49.6	9.07	36.8	6-10	0.19
P_3BIT template[68]	$A2_1am$	5.48	5.48	58.1	10.6	37.0	5-9	0.20
P_4BIT template[68]	$A2_1am$	5.49	5.49	66.2	12.1	37.3	4-7	0.26

To confirm the ability to incorporate PT powder into the Aurivillius structure, this

View Article Online
DOI: 10.1039/D5DT01206F

study replicated the method of PT templates preparation by sintering PT powder with plate-like $Bi_3Ti_4O_{12}$ (BIT) in molten NaCl salt. The relevant reaction equations are as follows:

$$Bi_3Ti_4O_{12} + 4PbTiO_3 = Pb_3Bi_4Ti_6O_{21} + PbTiO_3 \quad (4)$$

$$Bi_3Ti_4O_{12} + 5PbTiO_3 = Pb_4Bi_4Ti_7O_{24} + PbTiO_3 \quad (5).$$

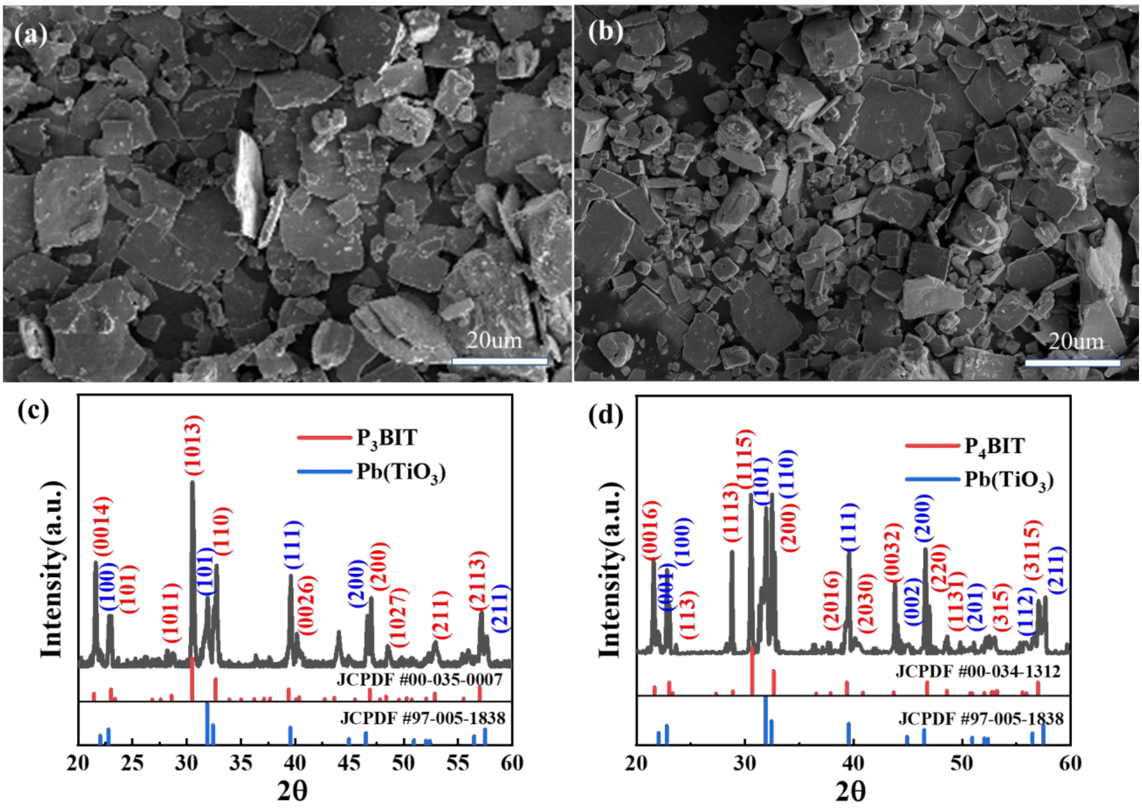

Fig. 11. (a-b) Morphologies of the synthesized products from BIT with 4 – 5 molar equivalents of $PbTiO_3$; (c-d) XRD patterns of the corresponding synthesized products.

Figures. 11(a-b) present the morphologies of the synthesized products from BIT with 4 - 5 molar equivalents of $PbTiO_3$. Both samples exhibit plate-like template structures, confirming successful incorporation of PT into the Aurivillius structure. As the PT content increases, intensified interlayer detachment promotes exfoliation and growth of the flaky templates, resulting in pronounced lamellar features. The XRD

View Article Online
DOI: 10.1039/D5DT01206F

patterns in Figures. 11(c-d) reveal the formation of P_3BIT and P_4BIT phases, along with characteristic peaks of the PT template. Notably, direct formation of P_4BIT did not occur when using 4 equivalents of PT, indicating that the substitution of Pb^{2+} for Bi^{3+} is a dynamic equilibrium process. The non-unidirectional nature of this disordered substitution further highlights the inherent instability in topochemical synthesis of PT templates.

3.3. The effect of BT and PT templates on textured PMN-30PT ceramics

3.3.1 The effect of formation energy of BT and PT templates on the epitaxial growth process of PMN-30PT ceramics

To investigate the effect of the BT/PT template on the textured PMN-30PT, we conducted a comprehensive analysis of the texture engineering process. This process involves thermally-driven grain growth, which is known to follow Arrhenius behavior[70]. The driving force behind this phenomenon is influenced by both the size of the matrix grains and the ratio of the template to matrix size. The activation energy required for TGG should be similar to that of regular grain growth, and can provide valuable insights into the mechanisms of matrix grains transport.

Since the texture evolution process originates from thermally activated grain growth, using a smaller matrix grain size would result in the production of denser ceramics with a higher texture quality. The driving force originates from the formation energy difference between the template and the matrix. In the case of the same matrix grains PMN-30PT, the difference in the formation energy of different templates leads to a difference in the TGG driving force. It is noteworthy that there is a significant difference in the formation energy between the BT template and the PT template. The formation energy of $PbTiO_3$, when formed from bulk PbO and TiO_2, is 0.36 eV, which is significantly lower than the formation energy of $BaTiO_3$ (3.23 eV) when both BT and PT are in the tetragonal phase. This suggests that PT has a lower thermal stability compared to BT. However, as the temperature rises and both PT and BT transition to the cubic phase, the formation energy of PT decreases to 0.3 eV, while the formation energy of BT remains at 3.20 eV. *B. Meyer*'s research indicates that both AO-terminated and TiO_2-terminated surfaces can be thermodynamically stable for the $BaTiO_3$ surface[71–73]. In contrast, for $PbTiO_3$, only the PbO surface termination is stable[71,72,74].

3.3.2. The effect of lattice parameter and physical properties of BT and PT templates on textured PMN-30PT ceramics

The TGG method involves the growth of matrix powder along the direction of the template. For effective growth, it is crucial that the lattice parameter of the template is similar to that of the matrix powder. This results in a uniform and compact structure. However, if there is a significant difference in lattice parameter, it can result in a disorderly arrangement of the atoms at the interface, which can negatively impact the formation of the textured structures.

Table. 4. The Lattice parameters and Physical properties of PMN-30PT,

View Article Online
DOI: 10.1039/D5DT01206F

BT template and PT template.

Ceramics	Lattice parameters					Morphologies		Physical properties		
Composition	Space group	a(Å)	c(Å)	c/a	△a/a (%)	Diameter (μm)	Thickness(μm)	T_m (℃)	ε_r	MP (℃)
PMN-30PT	P4mm	4.00	4.05	1.01	-	0.2	0.2	158.7	7000	
BT template	P4mm	3.99	4.03	1.01	0.25	5-10	0.5	120	1400	1625
PT template	P4mm	3.90	4.14	1.06	2.50	5-10	0.3	490	142	1286

Table. 4 displays the lattice parameters and physical properties of PMN-30PT matrix powders, BT template, and PT template. The c/a ratio of the PT template is significantly larger (1.06) than that of the BT template. As the temperature increases, the PT template undergoes a phase transition from tetragonal to cubic phase at the Curie temperature of 490 ℃. This transition causes the c/a ratio to change from 1.06 to 1, resulting in a significant volume contraction and reducing its cell volume from 63.28 Å^3 to 62.51 Å^3. This leads to internal strain and the formation of pores around the PT template [16]. The increased lattice parameter difference between the PT template and the matrix powder on the *a*-axis (2.50%) compared to the BT template (0.25%) makes the texturing process more challenging. Additionally, the melting point (MP) of PT (1286 ℃) is close to the sintering temperature of 1250 ℃, while the melting point (MP) of BT (1625 ℃) is significantly higher. This indicates that the stability of the PT template is poorer, making it more prone to decomposition. Furthermore, the thickness of the PT template is much lower than that of the BT template, further compromising its stability. These factors may contribute to the difficulty of achieving texture

View Article Online
DOI: 10.1039/D5DT01206F

engineering with the PT template.

3.3.3 A novel grain growth mechanism of BT and PT templates on textured PMN-30PT ceramics

In templated grain growth (TGG), texture development is primarily affected by the growth of the template particles rather than by template rearrangement or preferential texture development in the matrix. This correlation has been demonstrated across various sintering times, temperatures, and initial template concentrations[75]. A novel grain growth mechanism was proposed based on the fracture morphology of T_{BT} and T_{PT} piezoceramics. Figure. 12 illustrates the impact of grains transport direction on the growth and disappearance of template grains. In Figure. 12(a), when matrix grains diffuse into template grains, the template grains grow while the matrix grains disappear, resulting in the development of texture. However, in Figure. 12 (b), when the diffusion direction is reversed, the template grains disappear and textured ceramics cannot be achieved. During the sintering process, the growth of BT template grains is sacrificed in favor of matrix grains, leading to the formation of textures. The matrix grains grow along the BT template in the [001] direction, eventually forming a [001]-oriented "brick wall" structure. On the other hand, as the matrix grains grow at the expense of the PT template grains, the grain direction becomes random.

During the preparation of textured ceramics, the temperature can reach up to 1250 ℃, causing the volatilization of PbO. This leads to the decomposition of the

View Article Online
DOI: 10.1039/D5DT01206F

$PbTiO_3$ templates into PbO (g) and TiO_2, resulting in the presence of Pb-rich and Ti-rich phases near the template[26]. As a result, the matrix grains grow at the expense of the PT template grains, causing the PT template grains to disappear and preventing the formation of textured ceramics. However, the growth of BT template grains is sacrificed in favor of the matrix grains, resulting in the development of textures. The matrix grains grow along the BT template in the [001] direction, ultimately forming a [001]-oriented "brick wall" structure.

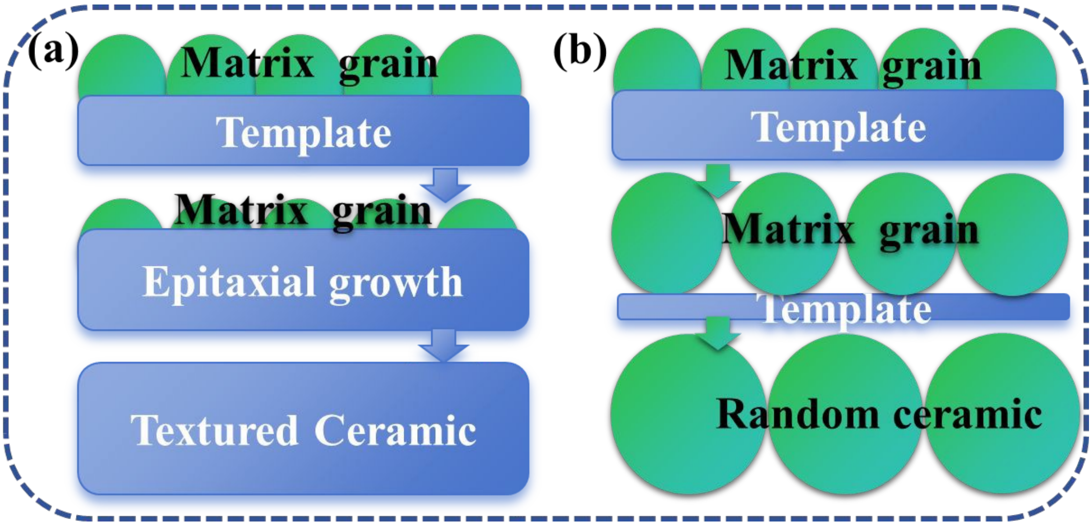

Fig. 12. Diagram of diffusion direction on the disappearance of (a) matrix grains and (b) template grains.

4. Conclusion

The PMN-30PT textured ceramics with BT and PT templates were fabricated, and their crystal structure, micromorphology, electric properties, and domain configuration were investigated. The textured ceramics with the BT and PT templates exhibited different properties. The T_{BT} sample had a texture quality of 91% (f = 91%) and a piezoelectric coefficient (d_{33}) value of 824 pC/N, while the T_{PT} sample had a

View Article Online
DOI: 10.1039/D5DT01206F

texture quality of 11% and a d_{33} value of 534 pC/N. These values are significantly higher than the d_{33} value of 489 pC/N observed in the random ceramic. In the T_{BT} sample, the domain structure is dominated by parallel striped domains, indicating a polarization direction towards to the same direction. In contrast, the T_{PT} sample, with a lower $[001]_c$ texture quality, shows an ordered fingerprint-like pattern dominating the domain structure.

The crystal structure, micromorphology, lattice parameter, and topological microcrystal conversion of BT and PT templates were also systematically investigated. Pure and shape BT templates were successfully obtained, while PT templates exhibited an uneven and hollow surface. It is worth noting that there were significant differences in the topological microcrystal conversion of BT and PT templates. This difference can be attributed to the structural instability of the PT template, caused by the absence of Pb^{2+} at the 4a position during the topochemical conversion process. The substitution of Bi^{3+} by Pb^{2+} induces chaotic displacement and interlayer detachment at the 4a position, thereby promoting the formation of PT nanosheets. Additionally, residual Bi^{3+} facilitates the generation of a more complex Aurivillius structure and allows PT templates to be embedded within this structure. The substitution of Pb^{2+} for Bi^{3+} is essentially a dynamic equilibrium process, which not only reflects the non-unidirectional nature of disordered substitution but also reveals the inherent instability in the topochemical synthesis of PT templates.

The effect of BT and PT templates on the textured PMN-30PT were investigated, and our analysis revealed that there are differences in the evolution of BT and PT

View Article Online
DOI: 10.1039/D5DT01206F

templates in texture engineering. The lower formation energy, the increased lattice parameter difference, and the lower melting point of PT templates make them more susceptible diffusion into the matrix grain, resulting in the growth of matrix grains at the expense of the PT template grains. As a result, the PT template grains disappear and textured ceramics cannot be obtained. On the other hand, the growth of BT template grains was sacrificed in favor of matrix grains, resulting in the formation of a [00*l*]-oriented "brick wall" structure.

Based on the analysis of textured PMN-30PT piezoceramic with PT templates， including texture quality, electrical properties, and domain structure, it is evident that achieving textured piezoelectric ceramics using PT templates is a challenging task. Furthermore, the physical properties of PT, its topochemical conversion process, and the texture engineering evolution process provide insight into the difficulties of achieving textured piezoceramics. Therefore, it can be concluded that the realization of textured piezoceramics using PT templates is a complex and demanding process.

CRediT authorship contribution statement

Xi Ouyang: Writing – original draft, Visualization, Validation, Methodology, Investigation, Formal analysis, Data curation, Conceptualization.

Manwen Yao: Supervision, Resources, Writing – review & editing, Supervision, Funding acquisition.

Tongqing Yang: Funding acquisition.

Conflicts of interest

View Article Online
DOI: 10.1039/D5DT01206F

There are no conflicts to declare.

Acknowledgement

This work was supported by the National Key R&D Program of China under grant number 2023YFE0198300 and National Natural Science Foundation of China under grant number 51872201.

Reference

(1) Messing, G. L.; Trolier-McKinstry, S.; Sabolsky, E. M.; Duran, C.; Kwon, S.; Brahmaroutu, B.; Park, P.; Yilmaz, H.; Rehrig, P. W.; Eitel, K. B.; Suvaci, E.; Seabaugh, M.; Oh, K. S. Templated Grain Growth of Textured Piezoelectric Ceramics. *Crit. Rev. Solid State Mater. Sci.* **2004**, *29* (2), 45–96. https://doi.org/10.1080/10408430490490905.

(2) Yang, S.; Li, J.; Liu, Y.; Wang, M.; Qiao, L.; Gao, X.; Chang, Y.; Du, H.; Xu, Z.; Zhang, S.; Li, F. Textured Ferroelectric Ceramics with High Electromechanical Coupling Factors over a Broad Temperature Range. *Nat. Commun.* **2021**, *12* (1), 1414. https://doi.org/10.1038/s41467-021-21673-8.

(3) Kimura, T.; Sakuma, Y.; Murata, M. Texture Development in Piezoelectric Ceramics by Templated Grain Growth Using Heterotemplates. *Journal of the European Ceramic Society* **2005**, *25* (12), 2227–2230. https://doi.org/10.1016/j.jeurceramsoc.2005.03.036.

(4) Brosnan, K. H.; Poterala, S. F.; Meyer, R. J.; Misture, S.; Messing, G. L. Templated Grain Growth of Textured PMN-28PT Using $SrTiO_3$ Templates. *Journal of the American Ceramic Society* **2009**, *92* (S1), S133–S139. https://doi.org/10.1111/j.1551-2916.2008.02628.x.

(5) Zhao, W.; Zhou, H.; Yan, Y.; Liu, D. Topochemical Synthesis of Plate-like $Na_{0.5}Bi_{0.5}TiO_3$ from Aurivillius Precursor. *J. Am. Ceram. Soc.* **2008**, *91* (4), 1322–1325. https://doi.org/10.1111/j.1551-2916.2007.02250.x.

(6) Bian, L.; Qi, X.; Li, K.; Yu, Y.; Liu, L.; Chang, Y.; Cao, W.; Dong, S. High-performance $[001]_c$-textured PNN-PZT Relaxor Ferroelectric Ceramics for Electromechanical Coupling Devices. *Adv. Funct. Mater.* **2020**, *30* (25), 2001846. https://doi.org/10.1002/adfm.202001846.

(7) Bian, L.; Kou, Q.; Liu, L.; Zheng, H.; Wang, N.; Qi, X.; Yang, B.; Cao, W. Enhancing the Temperature Stability of 0.42PNN-0.21PZ-0.37PT Ceramics through Texture Engineering. *ACS Appl. Mater. amp; Interfaces* **2022**, *14* (2), 3076–3083. https://doi.org/10.1021/acsami.1c21459.

(8) Jia, H.; Liang, Z.; Li, Z.; Li, F.; Wang, L. Texture Technique to Simultaneously Achieve Large Electric Field Induced Strain Response and Ultralow Hysteresis in BMT-PMN-PT Relaxor Ferroelectric Ceramics. *Scr. Mater.* **2022**, *209* (1), 114409. https://doi.org/10.1016/j.scriptamat.2021.114409.

(9) Andreeta, E. R. M.; Dos Santos, H. F. L.; Andreeta, M. R. B.; Lente, M. H.; Garcia, D.; Hernandes, A. C.; Eiras, J. A. Anisotropy on $SrTiO_3$ Templated Textured PMN–PT Monolithic Ceramics. *J. Eur. Ceram. Soc.* **2007**, *27* (6), 2463–2469. https://doi.org/10.1016/j.jeurceramsoc.2006.10.011.

(10) Li, T.; Wu, S.; Khan, A.; Scotch, A. M.; Chan, H. M.; Harmer, M. P. Heteroepitaxial Growth of Bulk Single-Crystal $Pb(Mg_{1/3}Nb_{2/3})O_3$–32 mol%$PbTiO_3$ from (111) $SrTiO_3$. *J. Mater. Res.* **1999**, *14* (8), 3189–3191. https://doi.org/10.1557/JMR.1999.0428.

(11) Richter, T.; Denneler, S.; Schuh, C.; Suvaci, E.; Moos, R. Textured PMN–PT and PMN–PZT. *J American Ceramic Society* **2008**, *91* (3), 929–933. https://doi.org/10.1111/j.1551-2916.2007.02216.x.

(12) Liu, L.; Yang, B.; Yang, S.; Kou, Q.; Xie, H.; Sun, Y.; Chang, Y.; Zhang, S.-T.; Li, F. Cu-Modified $Pb(Mg_{1/3}Nb_{2/3})O_3$-$PbZrO_3$-$PbTiO_3$ Textured Ceramics with Enhanced Electromechanical Properties and Improved Thermal Stability. *J. Eur. Ceram. Soc.* **2022**, *42* (6), 2743–2751. https://doi.org/10.1016/j.jeurceramsoc.2022.02.018.

(13) Brova, M. J.; Watson, B. H.; Walton, R. L.; Kupp, E.; Fanton, M. A.; Meyer, R. J.; Messing, G. L. Relationship between Composition and Electromechanical Properties of CuO-Doped Textured PYN-PMN-PT Ceramics. *Journal of the European Ceramic Society* **2021**, *41* (2), 1230–1235. https://doi.org/10.1016/j.jeurceramsoc.2020.09.048.

(14) Berksoy-Yavuz, A.; Savacı, U.; Turan, S.; Alkoy, S.; Mensur-Alkoy, E. Structural Features and Energy Harvester Device Applications of Textured 0.675PMN–0.325PT Piezoceramics. *J Mater Sci: Mater Electron* **2020**, *31* (12), 9650–9659. https://doi.org/10.1007/s10854-020-03510-8.

(15) Wei, D.; Yuan, Q.; Zhang, G.; Wang, H. Templated Grain Growth and Piezoelectric Properties of <001>-Textured PIN–PMN–PT Ceramics. *J. Mater. Res.* **2015**, *30* (14), 2144–2150. https://doi.org/10.1557/jmr.2015.189.

(16) Kim, E.-J.; Lee, T.-G.; Kim, D. S.; Kim, S.-W.; Yee, Y.-J.; Han, S. H.; Kang, H.-W.; Nahm, S. Textured $Pb(Zr,Ti)O_3$-$Pb[(Zn,Ni)_{1/3}Nb_{2/3}]O_3$ Multilayer Ceramics and Their Application to Piezoelectric Actuators. *Appl. Mater. Today* **2020**, *20* (1), 100695. https://doi.org/10.1016/j.apmt.2020.100695.

(17) Kwon, S.; Sabolsky, E. M.; Messing, G. L.; Trolier-McKinstry, S. High Strain, <001> Textured $0.675Pb(Mg_{1/3}Nb_{2/3})O_3$-$0.325PbTiO_3$ Ceramics: Templated Grain Growth and Piezoelectric Properties. *J American Ceramic Society* **2005**, *88* (2), 312–317. https://doi.org/10.1111/j.1551-2916.2005.00057.x.

(18) Kimura, T. Application of Texture Engineering to Piezoelectric Ceramics-A Review. *Journal of the Ceramic Society of Japan* **2006**, *114* (1325), 15–25. https://doi.org/10.2109/jcersj.114.15.

(19) Yan, Y.; Zhou, J. E.; Maurya, D.; Wang, Y. U.; Priya, S. Giant Piezoelectric Voltage Coefficient in Grain-Oriented Modified $PbTiO_3$ Material. *Nat. Commun.* **2016**, *7* (1), 13089. https://doi.org/10.1038/ncomms13089.

(20) Poterala, S. F.; Meyer Jr., R. J.; Messing, G. L. Synthesis of High Aspect Ratio $PbBi_4Ti_4O_{15}$ and Topochemical Conversion to $PbTiO_3$-Based Microplatelets: Synthesis of $PbBi_4Ti_4O_{15}$ and $PbTiO_3$-Based Microplatelets. *Journal of the American Ceramic Society* **2011**, *94* (8), 2323–2329. https://doi.org/10.1111/j.1551-2916.2010.04369.x.

(21) Poterala, S. F.; Trolier-McKinstry, S.; Meyer, R. J.; Messing, G. L. Processing, Texture Quality, and Piezoelectric Properties of $<001>_C$ Textured $(1\text{-}x)Pb(Mg_{1/3}Nb_{2/3})TiO_3$ - $xPbTiO_3$ Ceramics.

View Article Online
DOI: 10.1039/D5DT01206F

Journal of Applied Physics **2011**, *110* (1), 014105. https://doi.org/10.1063/1.3603045.

(22) Xu, G.; Bai, H.; Huang, X.; He, W.; Li, L.; Shen, G.; Han, G. Self-Assembled 3D Flower-like Perovskite $PbTiO_3$ Nanostructures and Their Application in the Catalytic Oxidation of CO. *J. Mater. Chem. A* **2015**, *3* (2), 547–554. https://doi.org/10.1039/C4TA04667F.

(23) Chao, C.; Ren, Z.; Yin, S.; Gong, S.; Yang, X.; Xu, G.; Li, X.; Shen, G.; Han, G. Hydrothermal Synthesis of Ferroelectric $PbTiO_3$ Nanoparticles with Dominant {001} Facets by Titanate Nanostructure. *CrystEngComm* **2013**, *15* (39), 8036. https://doi.org/10.1039/c3ce41248b.

(24) Deng, S.; Xu, G.; Bai, H.; Li, L.; Jiang, S.; Shen, G.; Han, G. Hydrothermal Synthesis of Single-Crystalline Perovskite $PbTiO_3$ Nanosheets with Dominant (001) Facets. *Inorg. Chem.* **2014**, *53* (20), 10937–10943. https://doi.org/10.1021/ic501180g.

(25) Na, Y.; Kwon, J.; Nahm, S.; Jeong, Y. H. Morphological Evolution of $PbTiO_3$ Microstructures Synthesized by Topochemical Microcrystal Conversion. *J. Am. Ceram. Soc.* **2022**, *105* (7), 4751–4762. https://doi.org/10.1111/jace.18435.

(26) Li, L.; Liu, J.; Cao, S.; Xu, J.; Wu, C.; Pawlikowska, E.; Szafran, M.; Gao, F. Microstructure Evolution and Reaction Mechanism of $Pb(Zr_{1/2}Ti_{1/2})O_3$-$Pb(Zn_{1/3}Nb_{2/3})O_3$–$Pb(Ni_{1/3}Nb_{2/3})O_3$ Piezoelectric Ceramics with Plate-like $PbTiO_3$ Template. *Ceramics International* **2021**, *47* (1), 470–478. https://doi.org/10.1016/j.ceramint.2020.08.154.

(27) Zhuang, C.; Yao, M.; Yao, X. Origin of High Comprehensive Electromechanical Properties of Novel Donor and Acceptor–Codoped PMN–30PT Ceramics. *Ceram. Int.* **2024**, *50* (1), 1428–1437. https://doi.org/10.1016/j.ceramint.2023.10.232.

(28) Yang, Y.; Sun, E.; Xu, Z.; Zheng, H.; Yang, B.; Zhang, R.; Cao, W. Sm and Mn Co-Doped PMN-PT Piezoelectric Ceramics: Defect Engineering Strategy to Achieve Large d_{33} and High q_m. *J. Mater. Sci. Technol.* **2023**, *137* (1), 143–151. https://doi.org/10.1016/j.jmst.2022.08.004.

(29) Li, J.; Li, J.; Wu, H.-H.; Zhou, O.; Chen, J.; Lookman, T.; Su, Y.; Qiao, L.; Bai, Y. Influence of Phase Transitions on Electrostrictive and Piezoelectric Characteristics in PMN–30PT Single Crystals. *ACS Appl. Mater. Interfaces* **2021**, *13* (32), 38467–38476. https://doi.org/10.1021/acsami.1c07714.

(30) Zhang, D.; Wang, L.; Li, L.; Sharma, P.; Seidel, J. Varied Domain Structures in $0.7Pb(Mg_{1/3}Nb_{2/3})O_3$-$0.3PbTiO_3$ Single Crystals. *Microstructures* **2023**, *3* (4). https://doi.org/10.20517/microstructures.2023.57.

(31) Zhang, D.; Li, L.; Wang, L.; Sando, D.; Sharma, P.; Seidel, J. Engineering Domain Variants in $0.7Pb(Mg_{1/3}Nb_{2/3})$–$0.3PbTiO_3$ Single Crystals Using High-frequency AC Poling. *Small Methods* **2024**, *8* (7), 2301257. https://doi.org/10.1002/smtd.202301257.

(32) Yan, Y.; Yang, L.; Zhou, Y.; Cho, K.-H.; Heo, J. S.; Priya, S. Enhanced Temperature Stability in 〈111〉 Textured Tetragonal $Pb(Mg_{1/3}Nb_{2/3})O_3$-$PbTiO_3$ Piezoelectric Ceramics. *J. Appl. Phys.* **2015**, *118* (10), 104101. https://doi.org/10.1063/1.4929958.

(33) Wang, Q.; Yao, M.; Lin, W.; Lin, J. Microstructure and Electrical Properties of Er-Doped $0.67Pb(Mg_{1/3}Nb_{2/3})O_3$-$0.33PbTiO_3$ Ceramics with $BaTiO_3$ Templates. *Ceram. Int.* **2023**, *49* (1), 437–442. https://doi.org/10.1016/j.ceramint.2022.09.009.

(34) Yan, Y.; Wang, Yu. U.; Priya, S. Electromechanical Behavior of [001]-Textured $Pb(Mg_{1/3}Nb_{2/3})O_3$-$PbTiO_3$ Ceramics. *Appl. Phys. Lett.* **2012**, *100* (19), 192905. https://doi.org/10.1063/1.4712563.

(35) Watson, B. H.; Brova, M. J.; Fanton, M.; Meyer, R. J.; Messing, G. L. Textured Mn-Doped

View Article Online
DOI: 10.1039/D5DT01206F

PIN-PMN-PT Ceramics: Harnessing Intrinsic Piezoelectricity for High-Power Transducer Applications. *J. Eur. Ceram. Soc.* **2021**, *41* (2), 1270–1279. https://doi.org/10.1016/j.jeurceramsoc.2020.07.071.

(36) Dong, Y.; Zhuang, C.; Ouyang, X.; Lin, W.; Yao, M.; Lin, J.; Yao, X. Investigations on Electric Properties and Domain Structures of Nd-Doped $0.70Pb(Mg_{1/3}Nb_{2/3})O_3$–$0.30PbTiO_3$ Relaxor Ferroelectric Ceramics with High Piezoelectric Properties. *J. Eur. Ceram. Soc.* **2023**, *43* (14), 6012–6020. https://doi.org/10.1016/j.jeurceramsoc.2023.06.014.

(37) Srinivasamurthy, K. M.; El-Denglawey, A.; Manjunatha, K.; Angadi V., J.; Oliveira, M. C.; Longo, E.; Lázaro, S. R.; Ribeiro, R. A. P. Observation of Dielectric Dispersion and Relaxation Behavior in Ni^{2+}-Substituted Cobalt Ferrite Nanoparticles. *J. Mater. Chem. C* **2022**, *10* (9), 3418–3428. https://doi.org/10.1039/D1TC05980G.

(38) Liu, H.; Dkhil, B. Effect of Resistivity Ratio on Energy Storage and Dielectric Relaxation Properties of 0–3 Dielectric Composites. *J. Mater. Sci.* **2017**, *52* (10), 6074–6080. https://doi.org/10.1007/s10853-017-0846-7.

(39) Samara, G. A.; Venturini, E. L.; Schmidt, V. H. Pressure-Induced Crossover from Long-to-Short-Range Order in $[Pb(Zn_{1/3}Nb_{2/3})O_3]_{0.905}(PbTiO_3)_{0.095}$ Single Crystal. *Appl. Phys. Lett.* **2000**, *76* (10), 1327–1329. https://doi.org/10.1063/1.126024.

(40) Liu, S.; Zhang, E.; Liu, S.; Li, D.; Li, Y.; Liu, Y.; Shen, Y.; Wang, S. Composition- and Pressure-induced Relaxor Ferroelectrics: First-principles Calculations and Landau-devonshire Theory. *J. Am. Ceram. Soc.* **2016**, *99* (10), 3336–3342. https://doi.org/10.1111/jace.14350.

(41) Leng, H.; Yan, Y.; Liu, H.; Fanton, M.; Meyer, R. J.; Priya, S. Design and Development of High-Power Piezoelectric Ceramics through Integration of Crystallographic Texturing and Acceptor-Doping. *Acta Mater.* **2021**, *206* (1), 116610. https://doi.org/10.1016/j.actamat.2020.116610.

(42) Rehrig, P. W.; Messing, G. L.; Trolier-McKinstry, S. Templated Grain Growth of Barium Titanate Single Crystals. *J. Am. Ceram. Soc.* **2000**, *83* (11), 2654–2660. https://doi.org/10.1111/j.1151-2916.2000.tb01610.x.

(43) Chang, Y.; Wu, J.; Liu, Z.; Sun, E.; Liu, L.; Kou, Q.; Li, F.; Yang, B.; Cao, W. Grain-Oriented Ferroelectric Ceramics with Single-Crystal-like Piezoelectric Properties and Low Texture Temperature. *ACS Appl. Mater. Interfaces* **2020**, *12* (34), 38415–38424. https://doi.org/10.1021/acsami.0c11680.

(44) Chang, Y.; Sun, Y.; Wu, J.; Wang, X.; Zhang, S.; Yang, B.; Messing, G. L.; Cao, W. Formation Mechanism of Highly $[001]_c$ Textured $Pb(In_{1/2}Nb_{1/2})O_3$-$Pb(Mg_{1/3}Nb_{2/3})O_3$-$PbTiO_3$ Relaxor Ferroelectric Ceramics with Giant Piezoelectricity. *J. Eur. Ceram. Soc.* **2016**, *36* (8), 1973–1981. https://doi.org/10.1016/j.jeurceramsoc.2016.02.030.

(45) Shi, W.; Zhang, H.; Liu, Y.; Bian, L.; Bi, W.; Deng, Y.; Yang, B. Improvement on q_m in High-Power Piezoelectric Ceramics through $[111]_c$ Texture Engineering. *J. Mater. Sci. Technol.* **2025**, *216* (1), 260–268. https://doi.org/10.1016/j.jmst.2024.07.035.

(46) Kou, Q.; Yang, B.; Sun, Y.; Yang, S.; Liu, L.; Xie, H.; Chang, Y.; Zhang, S.; Li, F. Tetragonal (Ba, Ca) (Zr, Ti)O_3 Textured Ceramics with Enhanced Piezoelectric Response and Superior Temperature Stability. *Journal of Materiomics* **2022**, *8* (2), 366–374. https://doi.org/10.1016/j.jmat.2021.08.006.

(47) Ganpule, C. S.; Roytburd, A. L.; Nagarajan, V.; Hill, B. K.; Ogale, S. B.; Williams, E. D.; Ramesh, R.; Scott, J. F. Polarization Relaxation Kinetics and 180° Domain Wall Dynamics in

View Article Online
DOI: 10.1039/D5DT01206F

Ferroelectric Thin Films. *Phys. Rev. B* **2001**, *65* (1), 14101. https://doi.org/10.1103/PhysRevB.65.014101.

(48) Gruverman, A.; Auciello, O.; Tokumoto, H. Imaging and Control of Domain Structures in Ferroelectric Thin Films via Scanning Force Microscopy. *Annu. Rev. Mater. Sci.* **1998**, *28* (1), 101–123. https://doi.org/10.1146/annurev.matsci.28.1.101.

(49) Luo, C.; Chang, W.-Y.; Gao, M.; Chang, C.-H.; Li, J.; Viehland, D.; Tian, J.; Jiang, X. Multi-Layered Domain Morphology in Relaxor Single Crystals with Nano-Patterned Composite Electrode. *Acta Mater.* **2020**, *182* (1), 10–17. https://doi.org/10.1016/j.actamat.2019.10.017.

(50) Bian, L.; Qi, X.; Li, K.; Fan, J.; Li, Z.; Sun, E.; Yang, B.; Dong, S.; Cao, W. High-Performance $Pb(Ni_{1/3}Nb_{2/3})O_3$-$PbZrO_3$-$PbTiO_3$ Ceramics with the Triple Point Composition. *Journal of the European Ceramic Society* **2021**, *41* (14), 6983–6990. https://doi.org/10.1016/j.jeurceramsoc.2021.07.034.

(51) Ahluwalia, R.; Lookman, T.; Saxena, A.; Cao, W. Domain-Size Dependence of Piezoelectric Properties of Ferroelectrics. *Phys. Rev. B* **2005**, *72* (1), 14112. https://doi.org/10.1103/PhysRevB.72.014112.

(52) Balke, N.; Bdikin, I.; Kalinin, S. V.; Kholkin, A. L. Electromechanical Imaging and Spectroscopy of Ferroelectric and Piezoelectric Materials: State of the Art and Prospects for the Future. *J. Am. Ceram. Soc.* **2009**, *92* (8), 1629–1647. https://doi.org/10.1111/j.1551-2916.2009.03240.x.

(53) *Scanning Probe Microscopy: Electrical and Electromechanical Phenomena at the Nanoscale*, 2nd ed.; Kalinin, S. V., Gruverman, A., Eds.; SpringerLink Bücher; Springer New York: New York, NY, 2007; Vol. 2. https://doi.org/10.1007/978-0-387-28668-6.

(54) Lai, Y.; Tian, G.; Cai, Y.; Kuai, W.; Gai, Z.; Chen, Y.; Du, J.; Zhao, M.; Zheng, L. Ultrahigh Strain and Superior Temperature Stability in Lead-Free Ceramics via Synergetic Texture Technique and Phase Structure Engineering. *J. Eur. Ceram. Soc.* **2024**, *44* (13), 7582–7589. https://doi.org/10.1016/j.jeurceramsoc.2024.05.022.

(55) Lu, G.; Zhao, Y.; Zhao, R.; Hao, J.; Bai, W.; Li, P.; Li, W.; Zhai, J. High Performance $(K,Na)NbO_3$-Based Textured Ceramics for Piezoelectric Energy Harvesting. *Ceram. Int.* **2024**, *50* (24), 54869–54877. https://doi.org/10.1016/j.ceramint.2024.10.279.

(56) Yan, Y.; Geng, L. D.; Liu, H.; Leng, H.; Li, X.; Wang, Y. U.; Priya, S. Near-Ideal Electromechanical Coupling in Textured Piezoelectric Ceramics. *Nat. Commun.* **2022**, *13* (1), 3565. https://doi.org/10.1038/s41467-022-31165-y.

(57) Liu, Q.; Zhang, Y.; Gao, J.; Zhou, Z.; Yang, D.; Lee, K.-Y.; Studer, A.; Hinterstein, M.; Wang, K.; Zhang, X.; Li, L.; Li, J.-F. Practical High-Performance Lead-Free Piezoelectrics: Structural Flexibility beyond Utilizing Multiphase Coexistence. *Natl. Sci. Rev.* **2020**, *7* (2), 355–365. https://doi.org/10.1093/nsr/nwz167.

(58) Sabolsky, E. M.; Trolier-McKinstry, S.; Messing, G. L. Dielectric and Piezoelectric Properties of 〈001〉 Fiber-Textured $0.675Pb(Mg_{1/3}Nb_{2/3})O_3$–$0.325PbTiO_3$ Ceramics. *Journal of Applied Physics* **2003**, *93* (7), 4072–4080. https://doi.org/10.1063/1.1554488.

(59) Kennedy, B. J.; Zhou, Q.; Ismunandar; Kubota, Y.; Kato, K. Cation Disorder and Phase Transitions in the Four-Layer Ferroelectric Aurivillius Phases $ABi_4Ti_4O_{15}$ (a=Ca, Sr, Ba, Pb). *J. Solid State Chem.* **2008**, *181* (6), 1377–1386. https://doi.org/10.1016/j.jssc.2008.02.015.

(60) Nalini, G.; Row, T. N. G. Structure Determination at Room Temperature and Phase Transition

View Article Online
DOI: 10.1039/D5DT01206F

Studies above T_c in $ABi_4Ti_4O_{15}$ (a = Ba, Sr or Pb). *Bull. Mater. Sci.* **2002**, *25* (4), 275–281. https://doi.org/10.1007/BF02704119.

(61) Ismunandar, B. Cation Disorder in the Ferroelectric Aurivillius Phase $PbBi_2Nb_2O_9$: An Anamolous Dispersion X-Ray Diffraction Study. *Solid State Ionics* **1998**, *112* (3–4), 281–289. https://doi.org/10.1016/S0167-2738(98)00222-7.

(62) Miura, K. Electronic Properties of Ferroelectric $SrBi_2Ta_2O_9$, $SrBi_2Nb_2O_9$, and $PbBi_2Nb_2O_9$ with Optimized Structures. *Appl. Phys. Lett.* **2002**, *80* (16), 2967–2969. https://doi.org/10.1063/1.1474607.

(63) Cohen, R. E. Origin of Ferroelectricity in Perovskite Oxides. *Nature* **1992**, *358* (6382), 136–138. https://doi.org/10.1038/358136a0.

(64) Hervoches, C. H.; Lightfoot, P. A Variable-Temperature Powder Neutron Diffraction Study of Ferroelectric $Bi_4Ti_3O_{12}$. *Chem. Mater.* **1999**, *11* (11), 3359–3364. https://doi.org/10.1021/cm991090d.

(65) Ismunandar; Kamiyama, T.; Hoshikawa, A.; Zhou, Q.; Kennedy, B. J. Structural Studies of Five Layer Aurivillius Oxides: $A_2Bi_4Ti_5O_{18}$ (a = Ca, Sr, Ba and Pb). *J. Neutron Res.* **2005**, *13* (1–3), 183–187. https://doi.org/10.1080/10238160412331299933.

(66) Fernández, J. F.; Caballero, A. C.; Villegas, M.; De Frutos, J.; Lascano, L. Relaxor Behavior of $Pb_xBi_4Ti_{3+x}O_{12+3x}$ (x=2,3) Aurivillius Ceramics. *Appl. Phys. Lett.* **2002**, *81* (25), 4811–4813. https://doi.org/10.1063/1.1529088.

(67) Tellier, J.; Boullay, P.; Mercurio, D. Crystal Structure of the Aurivillius Phases in the System $Bi_4Ti_3O_{12}$—$PbTiO_3$. *Z. Krist.* **2007**, *222* (5), 234–243. https://doi.org/10.1524/zkri.2007.222.5.234.

(68) Kikuchi, T. Stability of Layered Bismuth Compounds in Relation to the Structural Mismatch. *Materials Research Bulletin* **1979**, *14* (12), 1561–1569. https://doi.org/10.1016/0025-5408(72)90226-7.

(69) Tellier, J.; Boullay, P.; Manier, M.; Mercurio, D. A Comparative Study of the Aurivillius Phase Ferroelectrics $CaBi_4Ti_4O_{15}$ and $BaBi_4Ti_4O_{15}$. *J. Solid State Chem.* **2004**, *177* (6), 1829–1837. https://doi.org/10.1016/j.jssc.2004.01.008.

(70) Seabaugh, M. M.; Kerscht, I. H.; Messing, G. L. Texture Development by Templated Grain Growth in Liquid-phase-sintered A-alumina. *J. Am. Ceram. Soc.* **1997**, *80* (5), 1181–1188. https://doi.org/10.1111/j.1151-2916.1997.tb02961.x.

(71) Meyer, B.; Padilla, J.; Vanderbilt, D. Theory of $PbTiO_3$, $BaTiO_3$, and $SrTiO_3$ Surfaces. *Faraday Discuss.* **1999**, *114* (1), 395–405. https://doi.org/10.1039/a903029h.

(72) Eglitis, R. I. Comparative First-Principles Calculations of $SrTiO_3$, $BaTiO_3$, $PbTiO_3$ and $CaTiO_3$ (001), (011) and (111) Surfaces. *Ferroelectrics* **2015**, *483* (1), 53–67. https://doi.org/10.1080/00150193.2015.1058673.

(73) Padilla, J.; Vanderbilt, D. ***Ab Initio*** Study of $BaTiO_3$ Surfaces. *Phys. Rev. B* **1997**, *56* (3), 1625–1631. https://doi.org/10.1103/PhysRevB.56.1625.

(74) Eglitis, R. I.; Piskunov, S.; Heifets, E.; Kotomin, E. A.; Borstel, G. Ab Initio Study of the $SrTiO_3$, $BaTiO_3$ and $PbTiO_3$ (001) Surfaces. *Ceram. Int.* **2004**, *30* (7), 1989–1992. https://doi.org/10.1016/j.ceramint.2003.12.176.

(75) Zhou, J. E.; Yan, Y.; Priya, S.; Wang, Y. U. Computational Study of Textured Ferroelectric Polycrystals: Texture Development during Templated Grain Growth. *J. Appl. Phys.* **2017**, *121* (6), 64108. https://doi.org/10.1063/1.4976022.

View Article Online
DOI: 10.1039/D5DT01206F

View Article Online
DOI: 10.1039/D5DT01206F

Data Availability Statements

The data that support the findings of this study are openly available in Science Data Bank at https://www.scidb.cn. The hyperlinks to the relevant data are shown in Table. 1.

Table.1. The list of XRD, *P-E* hysteresis loops, dielectric constant (ε_r) and loss (*tanδ*) data

No.	Data	Sample	URL
1	XRD Patterns (Fig.1 in Manuscript at Page 6)	Random	https://download.scidb.cn/download?fileId=24655a4c9cc88cafd36ab9244e25ce7f&path=/V1/XRD-Random.txt&username=oyxi2004@163.com&fileName=XRD-Random.txt
2		T_{BT}	https://download.scidb.cn/download?fileId=d5ba062c75a54665c61bd180d0820502&path=/V1/XRD-TBT.TXT&username=oyxi2004@163.com&fileName=XRD-TBT.TXT
3		T_{PT}	https://download.scidb.cn/download?fileId=9a1003897a3fe769e134f9f474df9b1a&path=/V1/XRD-TPT.TXT&username=oyxi2004@163.com&fileName=XRD-TPT.TXT
4	XRD Patterns (Fig.5 in Manuscript at Page 16)	BT template	https://download.scidb.cn/download?fileId=75d3499719ce3418e58c2d906268a114&path=/V1/XRD-BT template.txt&username=oyxi2004@163.com&fileName=XRD-BT%20template.txt
5		PT template	https://download.scidb.cn/download?fileId=ade9ee7a11386311b71d31a8b2db453b&path=/V1/XRD-PT template.txt&username=oyxi2004@163.com&fileName=XRD-PT%20template.txt
6	(Fig.8(b) in Manuscript at Page 24)	P_3BIT template	https://download.scidb.cn/download?fileId=3b04de365e2f882975f4902d0619a5d1&path=/V1/XRD-PT Resalt.txt&username=oyxi2004@163.com&fileName=XRD-PT%20Resalt.txt
7	*P−E* hysteresis loops (Fig.3(f) in Manuscript at Page 9)	Random	https://download.scidb.cn/download?fileId=22eb4a99e26595051c1a524116aaaa99&path=/V1/PE-R-30KV.txt&username=oyxi2004@163.com&fileName=PE-R-30KV.txt
8		T_{BT}	https://download.scidb.cn/download?fileId=85789d61d10f27cfe287e2b6749d1b92&path=/V1/PE-TBT-30KV.txt&username=oyxi2004@163.com&fileName=PE-TBT-30KV.txt
9		T_{PT}	https://download.scidb.cn/download?fileId=ddeaa89ec0399f36d418b06c1b7bf2ed&path=/V1/PE-TPT-30KV.txt&username=oyxi2004@163.com&fileName

View Article Online
DOI: 10.1039/D5DT01206F

			=PE-TPT-30KV.txt
10	The dielectric constant (ε_r) and loss ($tan\delta$) as a function of temperature (ε_r) (Fig.3(a-c) in Manuscript at Page 9)	Random	https://download.scidb.cn/download?fileId=77d9d69ebabbd0dbd0994cc8b83fcd1b&path=/V1/Dielectric R.zip&username=oyxi2004@163.com&fileName=Dielectric%20R.zip
11		T_{BT}	https://download.scidb.cn/download?fileId=9ea07a1984b04155d82d361b80709291&path=/V1/Dielectric TBT.zip&username=oyxi2004@163.com&fileName=Dielectric%20TBT.zip
12		T_{PT}	https://download.scidb.cn/download?fileId=c8cbf5a6ff9251168ca8fb19ed9778da&path=/V1/Dielectric TPT.zip&username=oyxi2004@163.com&fileName=Dielectric%20TPT.zip
13	XRD patterns of the corresponding synthesized products (Fig. 11. (a-b)) in Manuscript at Page 28)	P3BIT	https://download.scidb.cn/download?fileId=33fa93abce3198727e0e09b36e18b56c&path=/V2/XRD-P3BIT.txt&username=oyxi2004@163.com&fileName=XRD-P3BIT.txt
14		P4BIT	https://download.scidb.cn/download?fileId=71744f0beb1e6e3d582543d593ee7d8c&path=/V2/XRD-P4BIT.txt&username=oyxi2004@163.com&fileName=XRD-P4BIT.txt